



HAL
open science

Wet spinning and 3D printing of supramolecular hydrogels in acid-base and dynamic conditions

Faniry Andriamiseza, Salomé Peters, Clément Roux, Nicolas Dietrich, Christophe Coudret, Juliette Fitremann

► **To cite this version:**

Faniry Andriamiseza, Salomé Peters, Clément Roux, Nicolas Dietrich, Christophe Coudret, et al.. Wet spinning and 3D printing of supramolecular hydrogels in acid-base and dynamic conditions. *Colloids and Surfaces A: Physicochemical and Engineering Aspects*, 2023, 673, pp.131765. 10.1016/j.colsurfa.2023.131765 . hal-04162938

HAL Id: hal-04162938

<https://hal.science/hal-04162938>

Submitted on 31 Jul 2023

HAL is a multi-disciplinary open access archive for the deposit and dissemination of scientific research documents, whether they are published or not. The documents may come from teaching and research institutions in France or abroad, or from public or private research centers.

L'archive ouverte pluridisciplinaire **HAL**, est destinée au dépôt et à la diffusion de documents scientifiques de niveau recherche, publiés ou non, émanant des établissements d'enseignement et de recherche français ou étrangers, des laboratoires publics ou privés.

This document is the author version of a work published in *Colloids and Surfaces A: Physicochemical and Engineering Aspects*, copyright ©Elsevier after peer review and technical editing by the publisher.

Final edited and published work available at: <https://doi.org/10.1016/j.colsurfa.2023.131765>

To cite this article:

Andriamiseza, F., Peters, S., Roux, C., Dietrich, N., Coudret, C., Fitremann, J., 2023. Wet spinning and 3D printing of supramolecular hydrogels in acid-base and dynamic conditions. *Colloids and Surfaces A: Physicochemical and Engineering Aspects* 673, 131765.

<https://doi.org/10.1016/j.colsurfa.2023.131765>

Wet spinning and 3D printing of supramolecular hydrogels in acid-base and dynamic conditions

Faniry Andriamiseza^{§,1}, Salomé Peters^{§,1}, Clément Roux¹, Nicolas Dietrich², Christophe Coudret¹, Juliette Fitremann^{*,1}

¹ Laboratoire des IMRCP, Université de Toulouse, CNRS UMR 5623, Université Toulouse III - Paul Sabatier, Toulouse, France

² Toulouse Biotechnology Institute, Université de Toulouse, CNRS, INRAE, INSA, Toulouse, France

Corresponding author:

Juliette Fitremann

juliette.fitremann@cnrs.fr

Tel +33 5 61 55 68 04

Laboratoire des IMRCP

Bâtiment 2R1, Université Paul Sabatier Toulouse III

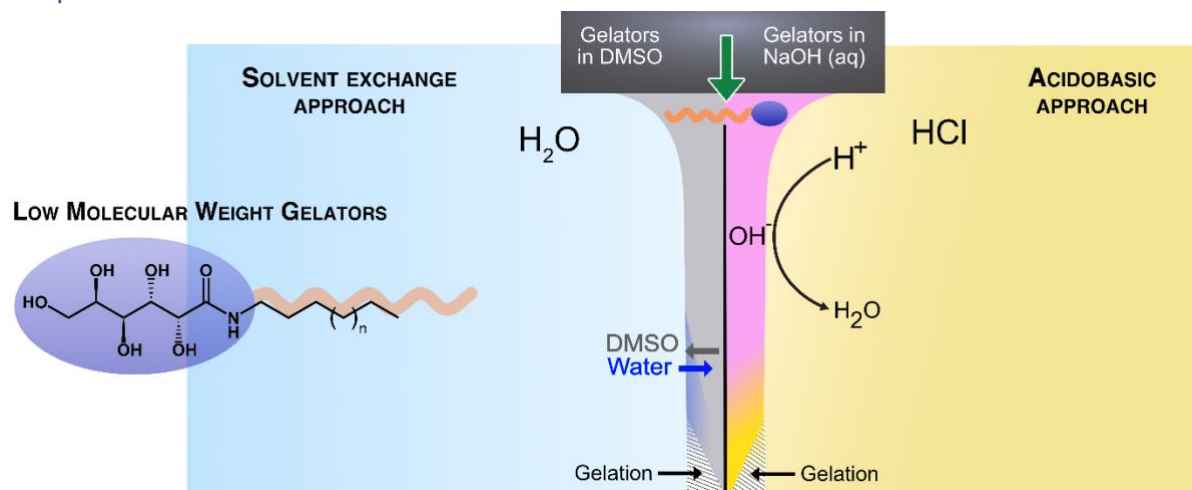
118 Route de Narbonne

31062 Toulouse cedex 9

France

§ equivalent contribution to the work

Graphical Abstract



Abstract

N-alkyl-D-galactonamides give biocompatible hydrogels that are very delicate and not injectable. To circumvent their mechanical fragility and the injectability issue, we have developed a method of injection based on solvent-water exchange. A solution of the gelator in a good solvent is injected vertically in a bath of water. The diffusion of water inside the solvent jet triggers the fast self-assembly of the N-alkyl-D-galactonamides into supramolecular fibers. It leads to the formation of well-defined gel filaments. We first used dimethylsulfoxide (DMSO) as the good solvent of N-alkyl-D-galactonamides. Then, we considered to get rid of this organic solvent by implementing an “all-aqueous method”, paving the way to green chemistry methods. Despite the fact that these molecules do not have conventional acid-base functions in water, N-alkyl-D-galactonamides can be deprotonated and solubilized in highly concentrated NaOH aqueous solutions. As with DMSO, the basic solution is denser than the solution in the bath. Thus, a well-defined vertical jet falls down when the solution is injected in an acidic aqueous solution. The neutralization of the base at the acid-base interface triggers the gelation and leads to the formation of well-defined gel filaments as well. The acid-base reaction at the interface has been visualized by colored pH indicators. With phenol red ($pK_a = 7.9$), a pink-to-yellow V-shaped “flame” transition is clearly observed. A similar transition from colorless-to-pink is observed with the pH indicator acid fuchsin, which $pK_a = 13$ is close to the N-heptyl-D-galactonamide pK_a . The distance from the nozzle of this transition zone is directly related to the injection rate, which is well-described by a model. We also applied this method to 3D printing, by a liquid-in-liquid direct writing. It gives well-resolved patterns. The opportunity to get noodles or 3D printed patterns made of single small molecules by acid-base exchange opens new perspectives. Notably, the supramolecular fibers could be used to support and direct the formation of inorganic materials with original microstructures.

keywords: molecular gel; hydrogel; supramolecular; LMWG; Low Molecular Weight Gelator, self-assembly; saccharide; carbohydrate; galactose; wet spinning; injectable; injection; noodle; thread; jet; liquid-liquid interface; interfacial reaction, mixing; 3D printing, pH, biocompatible

Introduction

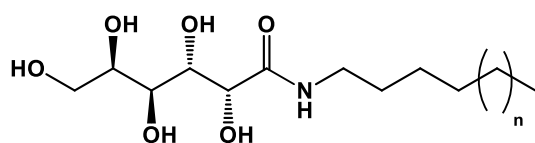
Some supramolecular gels, called "molecular gels", are non-polymer gels formed by the self-assembly of small molecules, most of the time into fibers or ribbons. These molecules are also called Low Molecular Weight Gelators (LMWG). They form a network of self-assembled objects, entangled on the long-range, which entraps a large amount of water (in the case of hydrogels)¹⁻²⁰ or an organic solvent (in the case of organogels)^{9,21-24}. The self-assembly is driven by the formation of bonds of low energy with high directionality, such as hydrogen bond, π - π -stacking and also involves Van-der-Waals and hydrophobic interactions. This topic also relates to supramolecular polymers, since the same mechanism of supramolecular assembly occurs. The difference lies in the number of dimensions in which the interactions take place. Interactions in molecular gels often develop in two dimensions, and the growth in one direction is most of the time more developed. It leads to the formation of fibers or ribbons with various aspect ratio. Interactions in supramolecular polymers are essentially mono-dimensional, leading to self-assembled objects of nanometric width.

The structure of the gelator drives the supramolecular assembly and the shape of the self-assembled objects (fibers, platelets, ribbons, helicity), their chirality (left-handed or right-handed helices)²⁵ and their dimensions (long, short, large, thick...)²⁰. The gelation conditions

also have an impact on the structure of the self-assembled objects and the resulting gel network. Gelation of LMWG can be triggered by different means (temperature, solvent shift, pH, enzymes^{8,26,27}, light²⁸, etc.) and subtle changes of these triggers can strongly change the properties of the self-assembled objects and the resulting gels^{16,29–38}.

Molecular hydrogels have been developed for various applications, including biomaterials^{11,34,39–44}, drug delivery¹⁰, 3D printing^{45,46}, scaffolds for mineralization^{47,48} etc. Because of the absence of covalent links between molecules, these hydrogels are quite fragile. However, taking advantage of this fragility to make ultrasoft and ultraporous hydrogels, sacrificial scaffolds or dynamic gels^{38,49} is interesting.

Different applications require the injection of the hydrogels. Typically, the introduction of a biomaterial in the body requires the injection of the hydrogels. 3D printing also involves injectable inks. For this reason, the following properties are highly desirable and searched: self-healing, fast rheological recovery (thixotropy or temperature sensitivity) or time-controlled gelation. However, some hydrogels however do not comply with any of these properties, which is the case for the carbohydrate alkylamides (Fig. 1). These molecules are however among the simplest molecular gelators, with easy synthesis compared with many other gelators. With the objective to make injectable these non-thixotropic and mechanically these fragile molecular hydrogels, we developed the wet-spinning gelation. In this method, a solution of the gelator in a good solvent is injected vertically in a bath of a non-solvent. The gelation is triggered by the diffusion of the non-solvent inside the jet of the gelator solution (Fig. 2). This method gives the opportunity to study the gelation phenomenon in new dynamic and interfacial conditions. These conditions are very different from static thermal gelation, where the gelator is solubilized by heating in the solvent, and the gelation occurs on cooling and at rest.



n=1: N-hexyl-D-galactonamide (GalC6)

n=2: N-heptyl-D-galactonamide (GalC7)

n=3: N-octyl-D-galactonamide (GalC8)

n=4: N-nonyl-D-galactonamide (GalC9)

Fig. 1 Gelator molecular structures and abbreviations

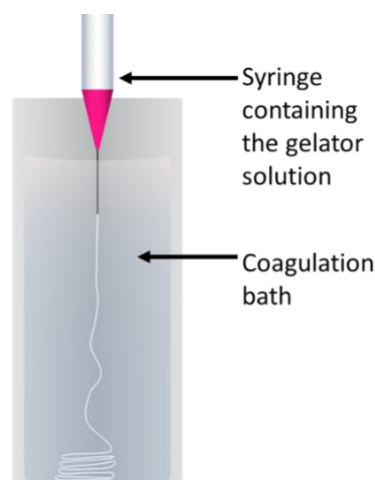


Fig. 2. Principle of wet spinning applied to the supramolecular gelators. The gelator solution is either a solution in DMSO or a solution in NaOH 8M. The coagulation bath is either water or a HCl solution, respectively. The exit of the nozzle is within the coagulation bath.

We applied this method to a library of carbohydrate-derived molecular gels^{34,36,45,46,50,51–54}. The gelator is dissolved in dimethylsulfoxide (DMSO). The diffusion of water within the liquid jet of DMSO-gelator solution triggers the self-assembly of the gelator into supramolecular fibers, ribbons, platelets or aggregates. It resulted in the formation of continuous coils of highly hydrated gel filaments. In this paper, the first objective was to extend the method applied to N-heptyl-D-galactonamide to three other gelators of the same family, N-hexyl, N-octyl and N-nonyl-D-galactonamides (Fig. 1). The second objective was to find “aqueous-only” conditions to implement this method. It gets rid of the organic solvent and provide more eco-friendly conditions. Because many inorganic species are formed by precipitation in aqueous conditions at various pH, these conditions also open perspectives for the shaping and the injection of inorganic species. Such conditions are implemented notably to form mineral tubes and “chemical gardens”⁵⁵ (metal hydroxide and sulfides⁵⁶, phosphates⁵⁷, silicates⁵⁸) or tubes of polymers which coagulate under acid-base conditions (chitosan^{59,60}).

However, N-alkyl-D-galactonamides are neutral polyhydroxylated species poorly soluble in water. To make them soluble in water solution, complexation with boronic acid is one well-known method to reversibly introduce a charge on a neutral carbohydrate, in basic conditions. But we also found that adding a base in the absence of boronic acid also leads to the solubilization of the alkyl-galactonamides. Given the structure similarity between GalC7 and galactitol (dulcitol), of which $pK_a = 13.43$ ⁶¹, GalC7 is likely to be deprotonated at high pH, which explains its solubility in water in these conditions. We thus studied the possibility of implementing the wet spinning by pH shift, by injecting a basic aqueous solution of N-heptyl-D-galactonamide into an acidic aqueous solution. By adjusting the parameters, the formation of a well-defined continuous gel filaments has been observed as well. The pH changes all along the jet have been monitored by the addition of a colored pH indicator and compared to the gelation onset. It gave an insight into the mechanism of solvent exchange during the wet spinning process as a function of the wet spinning parameters (injection rate, concentration, pH) that will be useful when it will come to applying this method to mineralization.

Results and discussion

1- Wet spinning of N-hexyl, N-octyl and N-nonyl-D-galactonamides by DMSO / water exchange

1.1 – Phase diagram

In a previous work, we demonstrated that a molecular hydrogel, N-heptyl-D-galactonamide (GalC7) can be wet spun into well-defined hydrogels filaments by wet spinning. In order to extend the family of galactonamides hydrogels that forms hydrogel filaments by wet spinning, N-hexyl, N-octyl and N-nonyl-D-galactonamides (referred to as GalC6, GalC8, GalC9 in the following text, see Fig. 1) have been tested. For this purpose, solutions of GalC6, GalC8, GalC9 in DMSO, with concentrations between 50-100 mg/mL (0.18-0.36 mol.L⁻¹) for GalC6 and between 10-40 mg/mL (0.03-0.13 mol.L⁻¹) for GalC8 and GalC9 have been injected in a bath of water. The injection rate is set between 5 μ L/min and 150 μ L/min. To get a continuous filament instead of droplets, the nozzle exit is placed below the air/water interface. Depending on the concentration and the injection rate, 3 main results are obtained, which are reported in a

diagram (Fig. 3). When the injection rate is too low and/or the concentration too high, the gelation occurs too quickly at the exit of the nozzle, resulting in a clog (red marks, photo of the gel clog in the red frame). When the injection rate is too fast, the contact time of the DMSO / gelator solution with water is not long enough to trigger the full gelation before it reaches the bottom of the tank. When the concentration is too low, the intertwining of the supramolecular fibers is not sufficient to provide a cohesive gel. In both conditions, the gel forms without any particular shape at the bottom of the tank (blue marks, gel in the blue frame). In intermediate conditions of concentration and injection rate, the diffusion of water inside the DMSO jet triggers the gelation during the fall, to a sufficient extent to get a continuous filament of gel (green marks, gel filament and coil in the green frame). A continuum is observed which depends on the injection rate: white and thin filaments are obtained at a lower injection rate, because the diffusion of water and thus the gel setting are complete in those cases (light green marks). Transparent filament and coils, which are larger, are obtained at a higher injection rate and turn white with time: in this case, we hypothesize that a thin shell of gel is already formed during the fall and enables the formation of a well-defined coil and that the full gelation occurs later (dark green marks). The suitable concentration to get gel filaments increases as the chain length decreases, from GalC9 to GalC6. Typical suitable concentrations for wet spinning at 10-20 $\mu\text{L}/\text{min}$ are 10 mg/mL (0.03 mol.L^{-1}) for GalC9 while it is 30 mg/mL (0.10 mol.L^{-1}) for GalC8, 40 mg/mL for GalC7 (0.14 mol.L^{-1}) and 100 mg/mL (0.36 mol.L^{-1}) for GalC6. This progression is related to the fact that the solubility increases when the chain length decreases: a higher gelator concentration is needed to get a gel with the more soluble gelator, such as GalC6 and a lower gelator concentration is required to avoid clogging for the less soluble ones, such as GalC9. The persistence of the filament in the bath is also related to the solubility of the gelator. Once the filament is formed, the gelator concentration within the filament is not at equilibrium. As a consequence, the filament slowly dissolves in the water bath (reduced to 10 mL), until the concentration reaches the solubility limit. GalC6 filaments dissolve quickly, within a few minutes while GalC8 at concentration over 40 mg/mL and GalC9 filaments at concentration over 20 mg/mL are not dissolved after 3 months. GalC8 filaments tend to undergo a morphological transformation to crystals, as it was observed in the case of GalC7³⁶.

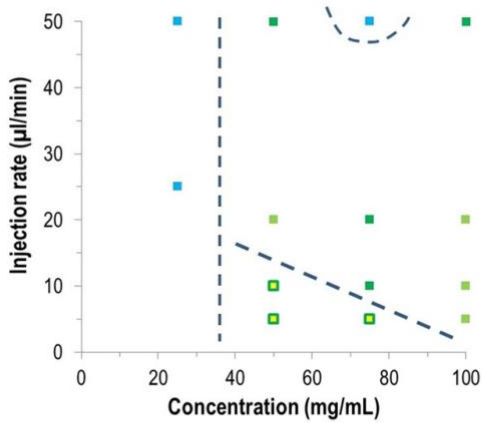
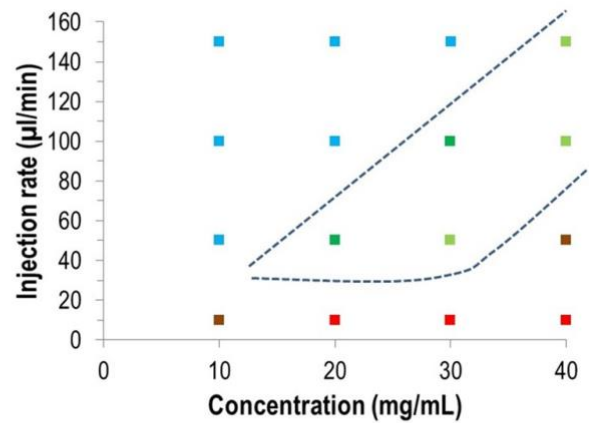
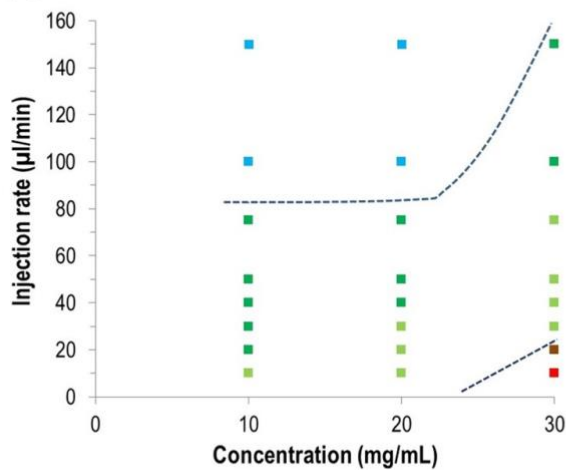
(a)-GalC6**(b)-GalC8****(c)-GalC9**

Fig. 3. Wet spinning diagram for (a) *N*-hexyl-*D*-galactonamide (GalC6), (b) *N*-octyl-*D*-galactonamide (GalC8), (c) *N*-nonyl-*D*-galactonamide (GalC9). **Blue**: gelation in flakes at the bottom of the tank; **light green**: white gel filament and coil during the fall; **dark green**: transparent gel filament and coil, which turns white within a few minutes after formation; **dark green open square**: very thin filament which stacks in thin columns; **brown**: filament with intermittent clogs; **red**: clogs at the nozzle exit. Examples of gels obtained in different conditions (with GalC9): photo with blue frame: 20 mg/mL; 100 µL/min; with green frame: 30 mg/mL; 50 µL/min; with red frame: 30 mg/mL; 10 µL/min.

1.2. Microstructure of wet spun filaments

The microstructure of the wet spun filament has been investigated by cryoSEM. In the case of GalC6, the microstructure is formed by the assembly of spherulites of fibers of around 10-30 µm, entangled to each other thanks to long fibers (Fig. 4a). In the case of GalC8, the fibers are also organized radially on a longer scale. Filament diameter is around 200 µm measured by optical microscopy or by video recording for the three gelators. For GalC8, the section observed in cryoSEM is around 100 µm (Fig. 4b). Both optical microscopy of the wet filament (Fig. 4d) and cryo electron microscopy tend to show that the radial arrangement spans the whole section in the case of GalC8. The dark brown backbone observed in filaments of GalC8 is not seen with other gelators and could be explained by the radial organization of the fibers. The long range

radial organization has also been observed by cryoSEM in the case of N-heptyl-D-galactonamide wet spinning³⁶. In the case of GalC9 the fibers are much shorter and larger and no particular organization has been observed (Fig 3c). A possible explanation of this difference in microstructure relies on the difference of solubility of the gelators^{34,45}. GalC6 is slightly soluble in water and gelation should not occur immediately in contact with water. Thus, nucleation occurs at any position within the jet, followed by the growth in the shape of spherulites. Interestingly, depletion zones where the density of fibers is low are clearly observed. It can be explained by the same principles as reaction-diffusion patterns. The consumption of the gelator by the growing spherulites decreases the concentration of gelator below the critical aggregation concentration all around, explaining the depletion area^{16,62,63}. Conversely, GalC8 is very poorly soluble in water. Nucleation should occur very quickly as soon as the water content mixed with DMSO is high, at the periphery of the jet. Nucleating points then grow toward the center of the jet. This organized growth would be either due to the water diffusion gradient or related to a fingering phenomenon at the liquid-liquid interface⁶⁴. Finally, GalC9 is so poorly soluble in water that its precipitation is completely disordered.

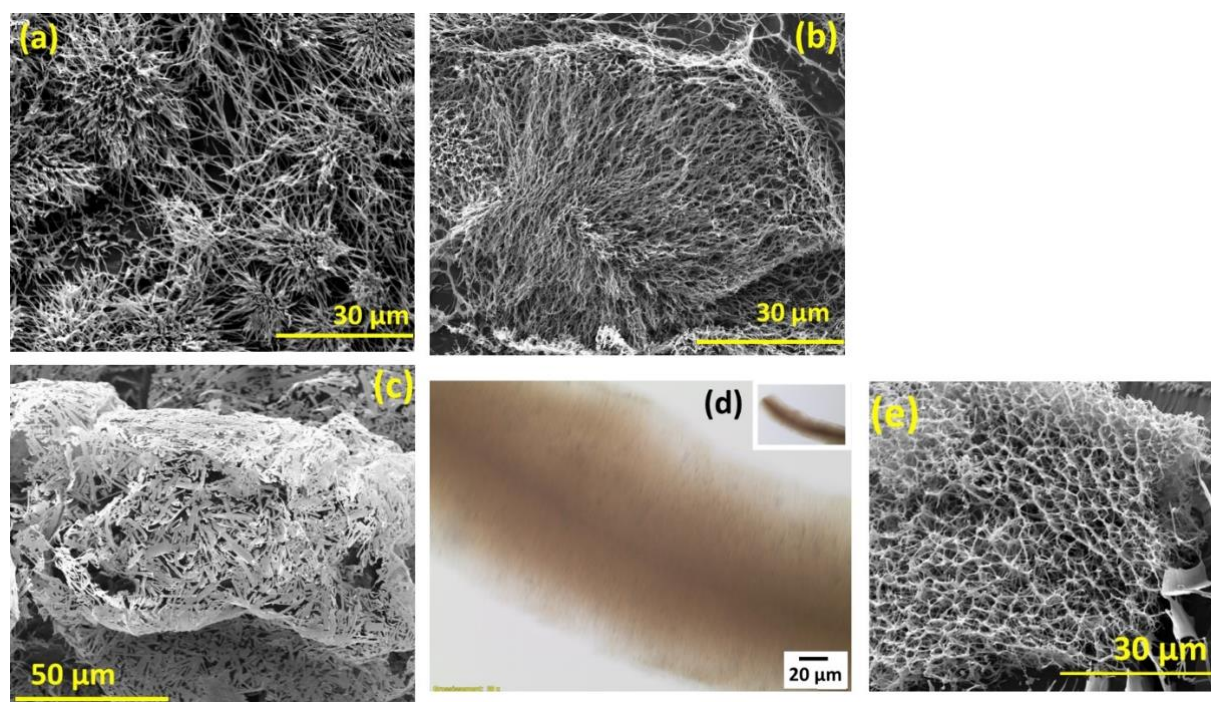


Fig. 4: Cryo-electronic microscopy of a gel filament prepared by wet spinning a solution of GalCn in DMSO in a bath of water: (a) GalC6: 100 mg/mL, 20 μ L/min; (b) GalC8: 25 mg/mL, 25 μ L/min; (c) GalC9: 10mg/mL, 20 μ L/min. (d) Optical microscopy of a filament of GalC8 50 mg/mL, 50 μ L/min (with other gelators, the brown "backbone" is not observed, which could be the sign of a radial organization throughout the filament). (e) Cryo-electronic microscopy of a gel filament prepared by wet spinning a solution of GalC7 dissolved in NaOH 8 mol.L⁻¹ in a bath of HCl 1.4 mol.L⁻¹. More images in SI-1.

2- Wet spinning in acid-base aqueous conditions

In order to get rid of the organic solvent, wet spinning in only aqueous conditions has been searched. It opens perspectives for green chemistry and will enable using the molecular gels as a support to extrude and shape inorganic species into filament. Galactonamides are not supposed to be sensitive to deprotonation since they have only hydroxyl groups. However neutral carbohydrates and polyols can be deprotonated at high pH (e.g. pKa of dulcitol =

galactitol is 13.43⁶¹). The resulting negatively charged molecule is likely to be soluble in water in these conditions. Conversely, the protonation should trigger the gelation. This assumption has been tested here with N-heptyl-D-galactonamide GalC7 as the gelator.

2.1- Dissolution and stability of N-heptyl-D-galactonamide in concentrated NaOH solutions

The first attempts confirmed that GalC7 can be solubilized at room temperature in basic solution. Gradual increase of the NaOH concentration shows that solubilization is fast enough and complete when the concentration of NaOH reaches 8 mol.L⁻¹. At a lower concentration, solubilization is incomplete or requires heating which is likely to degrade the molecule. Since the conditions of the experiment are quite harsh, a prior study of the stability of the gelator was conducted using NMR spectroscopy. The gelator was solubilized in an aqueous solution of NaOH 8 mol.L⁻¹ for 5, 10, 30 and 60 minutes. When GalC7 is left for an hour in NaOH, small peaks were observed in the NMR spectrum at 2.7 ppm (Fig. SI.2) corresponding to the heptylammonium⁴⁵, due to the hydrolysis of the amide bond. Thus, in the conditions used in this study (i.e. no heating and injection within 45 minutes after the preparation of the solution), GalC7 is stable during the experiment timescale.

2.2- Gelation and wet spinning in acid-base conditions

The basic solution of GalC7 is injected into an acidic coagulation bath with the end of the needle immersed in the bath (Fig. 5). Since the basic solution is denser than the coagulation bath solution, a well-defined liquid jet falls vertically (density of GalC7 0.2 mol.L⁻¹ in NaOH 8 mol.L⁻¹: 1.44 g/mL; density NaOH 8M: 1.23 g/mL; density HCl 2 mol.L⁻¹: 1.04 g/mL; density DMSO: 1.10 g/mL). In contact with the acidic solution, the deprotonated galactonamide returns to its neutral form, which is poorly soluble in water. It triggers its self-assembly in supramolecular fibers and the gelation. Preliminary experiments have shown that the injection of the basic solution of GalC7 in neutral water does not lead to the formation of a gel filament: the gelation does not occur during the fall, because the neutralization does not proceed fast enough in these conditions. Thus, wet spinning has been carried out in hydrochloric acid (HCl) aqueous solutions to increase the neutralization rate and trigger the gelation during the fall. The concentration of GalC7 is set between 65 and 80 mg/mL (0.25 mol.L⁻¹ ±10%, 0.22 to 0.27 mol.L⁻¹). In this range, a well-shaped filament is formed without clogs. The molar ratio of NaOH 8 mol.L⁻¹ to GalC7 is 32 equivalents. The injection rate varied from 2 to 8 μL/min. The concentration of HCl varied first from 0.01 mol.L⁻¹ to 8 mol.L⁻¹ to identify the range in which a gel filament is formed. A concentration lower than 0.4 mol.L⁻¹ does not trigger the gelation fast enough to provide a continuous filament. The formation of continuous gel filaments occurs in HCl 2 mol.L⁻¹ (Table 1). HCl concentration at 4 mol.L⁻¹ and above leads to the formation of clogs, because the acid-base neutralization of the gelator occurs very early at the exit of the needle. Further experiments were thus carried out in HCl solutions of concentration between 0.5 to 2 mol.L⁻¹. The formation of the gel filament has been monitored by a camera. The sol-gel transition within the jet can be visualized directly in white light showing the formation of the white gel, progressing from the outer to the inner of the gel and a filament diameter of around 160 μm (Fig. 5a). The "flame tip" where the whole jet turns white can be considered as the "gelation point".

HCl concentration (mol/L)	Formation of gel filament	Observation of color change
0.01	No	No
0.1	No	No
0.4	No	Yes
2	Yes	Yes
4	Clog	Clog
8	Clog	Clog

Table 1. Wet spinning results as a function of HCl concentration in the bath. Concentration GalC7 = 0.25 mol.L⁻¹. Injection rate = 5 μL/min.

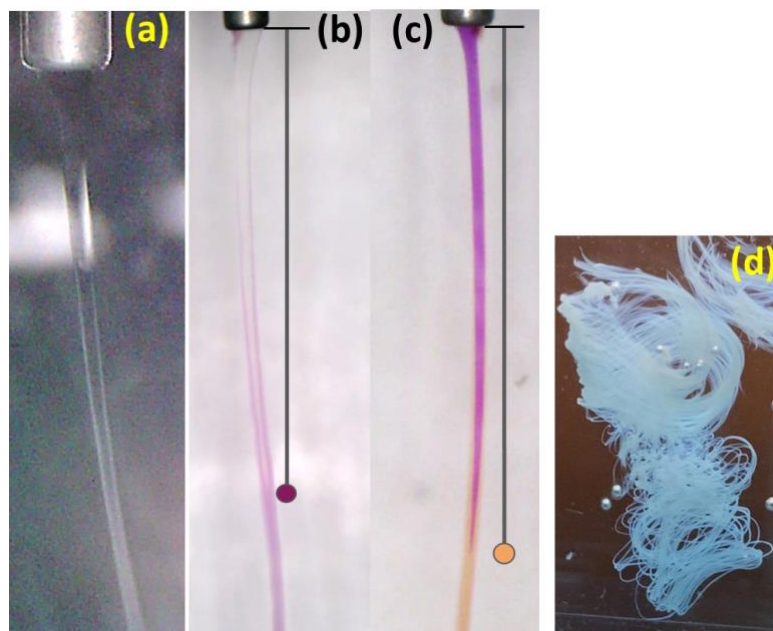


Fig 5: (a) Visualization of the gel shell formation and the gelation point without pH indicator (HCl 1.33 mol.L⁻¹, 4 μL/min). (b) Visualization of the color change of (b) acid fuchsin and (c) phenol red. (d) gel coil obtained in acid-base conditions.

In order to also visualize the pH change within the jet, colored pH indicators have been added to the GalC7 basic solution. Phenol red has been added as a medium-range pH indicator (pKa = 7.9, dark pink to yellow) and acid fuchsin has been selected as a high pKa indicator (pKa = 13, colorless to pink). The latter pKa is close to the pKa expected for GalC7. We expect that the neutralization of the gelator molecules would occur at the same pH as acid fuchsin and thus follow the same trend. The color change is clearly seen for both indicators (Fig 5b,c). As it has been observed directly with the filament formation in white light without dye (Fig 5a) a gradual change from the outer to the inner part of the jet is also observed, forming a "flame". The "flame tip" where the whole jet turns white or changes color will be called the "color switch point" in the rest of the article. The distance of the color switch point to the exit of the nozzle has been plotted as a function of HCl concentration and injection rate for both indicators (Figs. 6 and 7). The position of the color change fluctuates to some extent in the range of ±5 mm during the same injection for identical conditions, leading to the dispersion of the data (Fig. 6). This dispersion may be related either to jet and interfacial instabilities and/or to pump cycles. Despite the dispersion, clear trends can be extracted from these measurements highlighting the effect of the injection rate and the acid concentration in the coagulation bath.

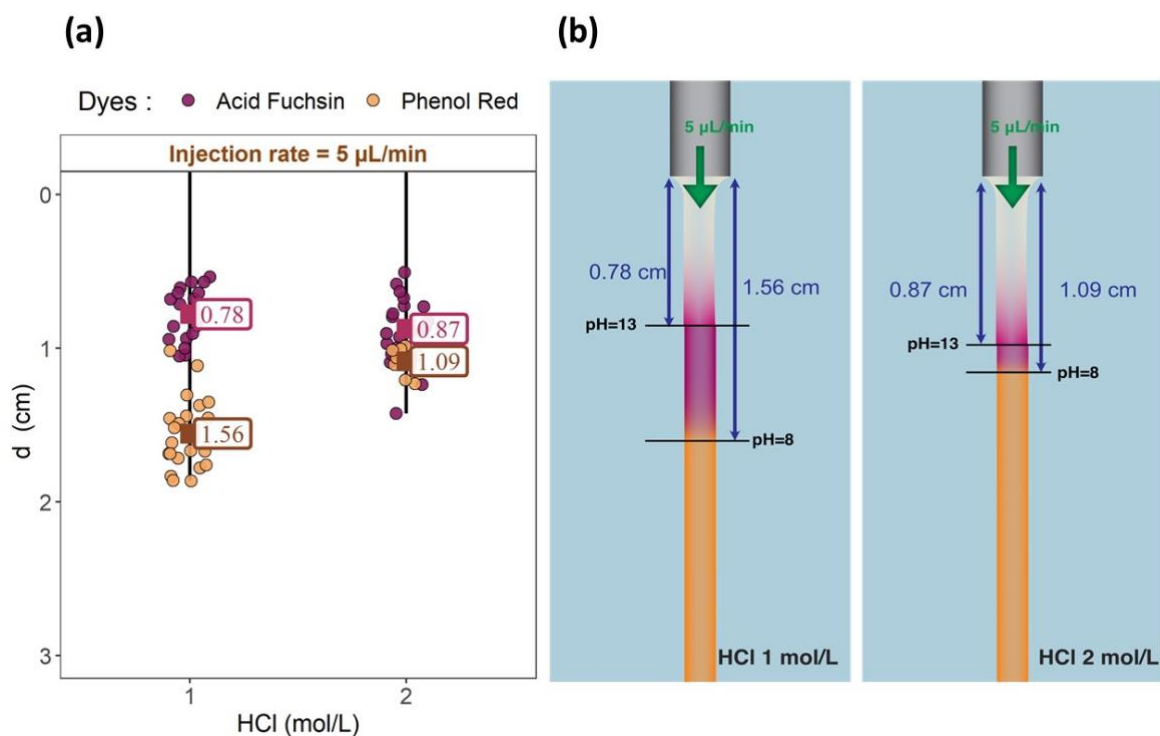


Fig. 6. Scheme illustrating the position of the color switch point for both indicators, phenol red and acid fuchsin. (b) theoretical scheme (the two indicators are superimposed) explaining how the color switch point is expected to change depending on the indicator's pKa and HCl concentration. (a) illustrates the dispersion of the experimental data. Despite the dispersion, it follows the expected trend.

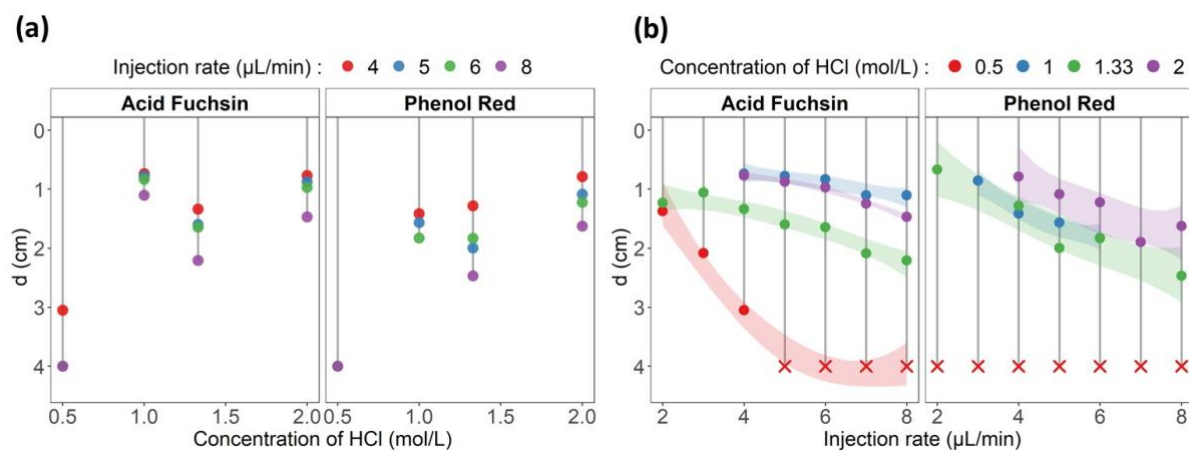


Fig. 7: (a) Effect of HCl concentration on the color switch point, at different injection rates; (b) Effect of the injection rate on the color switch point, at different HCl concentrations. Each circle represents the mean distance at which the color change was observed for both indicators, acid fuchsin and phenol red. The colored zones correspond to the 95% confidence interval. Red crosses correspond to conditions in which the color change does not occur before reaching the bottom of the vial (Full data in SI).

The color switch point is closer to the needle when the concentration of HCl increases, for both pH indicators. A strong variation in the position of this color switch is observed for $[HCl] \leq 1$ mol.L⁻¹ and then it reaches a plateau when $[HCl] \geq 1$ mol.L⁻¹. The color switch point is also sensitive to the injection rate: the color switch occurs lower when the injection rate is higher. These observations can be explained by the volume of basic solution (the jet) and acidic solution (the bath) that mixed at the interface during the fall. The amount of H⁺ mixed with OH⁻ depends on the injection rate and on HCl concentration. It reaches the saturation when $[HCl] \geq 1$ mol.L⁻¹.

More in details, the reaction of H^+ with OH^- occurs when the solution of acid is mixed with the basic solution of the jet. We assume that the mixing takes the form of an interfacial mixing phenomenon, as seen in two-dimensional Hele-Shaw cells, rather than a diffusion phenomenon of H^+ and/or a counter diffusion of OH^- . If we consider a differential volume (or fluid parcel) " V_{dz} " of the jet that just emerged from the nozzle. This volume is exposed to the solution of acid. The mixing of the H^+ solution with the OH^- solution in the jet neutralizes a given amount of the OH^- contained in this differential volume V_{dz} . Then the elementary volume moves to the next position, and the same amount of OH^- is again neutralized. We first hypothesize that the amount of H^+ that enters the jet is constant regardless of where V_{dz} is located. Since the volume of the bath is significantly greater than the volume of the jet and considering the high concentration of HCl in the bath, we also assume that the interface is not depleted in H^+ (at least when $[HCl] \geq 1 \text{ mol.L}^{-1}$). The amount of H^+ that reacts with V_{dz} depends on the residence time of V_{dz} in the liquid column represented by the bath height. Thus, when the flow rate is low a higher amount of the H^+ solution will mix with V_{dz} all along its trip downward. As a consequence, all OH^- (and the other bases, namely deprotonated GalC7 and the pH indicator) will be neutralized at a position closer to the nozzle when the flow rate is slower. Conversely, all the OH^- will be neutralized at a position more remote to the nozzle when the flow rate is faster. This effect is observed from $[HCl] = 0.5$ to 1 mol.L^{-1} , then a plateau is observed. Over 1 mol.L^{-1} , the amount of H^+ reacting with V_{dz} no longer depends on the concentration of HCl. It means that the limiting rate for neutralizing OH^- is not the diffusion or mixing of H^+ with the OH^- jet anymore. This qualitative model explains well the variations of the color change observed in the wet spinning conditions.

Another way to highlight this trend is to plot the position of the color change as a function of the injection rate (Fig. 7b). This representation clearly shows that the color change occurs lower and lower when the injection rate is higher. The comparison of the two pH indicators is also significant: the color switch of acid fuchsin ($pK_a = 13$) occurs higher compared to the color switch of phenol red ($pK_a = 7.9$). It is consistent with the pK_a values (Fig. 6b), since the neutralization of the base in the fluid parcel up to $pH = 13$ will occur earlier than its neutralization up to $pH = 7.9$. Thus the color change of acid fuchsin occurs at a shorter distance compared to phenol red in all the conditions up to $[HCl] = 2 \text{ mol.L}^{-1}$. At $[HCl] = 2 \text{ mol.L}^{-1}$, the color switch of both pH indicators occurs nearly at the same distance, because the neutralization of the base with the acid occurs earlier.

Correlation between the "gelation point" observed in the absence of a pH indicator (Fig. 5a) and the "color switch point" of the jets with indicators has been attempted. However, because of the fluctuation of the jet out of the focus plane, catching the images of the "gelation point" is much more difficult compared to colored solutions. In the conditions where we were able to measure it, the gelation point occurs between 0.25 to 0.5 cm (at $4 \mu\text{L}/\text{min}$, $HCl 1.33 \text{ mol.L}^{-1}$). Thus, it occurs earlier than the phenol red and acid fuchsin switch (1 to 1.5 cm at $4 \mu\text{L}/\text{min}$, $HCl 1.33 \text{ mol.L}^{-1}$). This result is in accordance with a pK_a of GalC7 higher than both phenol red and acid fuchsin pK_a . From a practical point of view, in order to get a well-shaped gel filament, the best conditions are $1 \text{ mol.L}^{-1} \leq [HCl] \leq 2 \text{ mol.L}^{-1}$, an injection rate within 2 to 8 $\mu\text{L}/\text{min}$ and a concentration of GalC7 within 0.2 to 0.3 mol.L^{-1} . When the concentration of HCl $\geq 1 \text{ mol.L}^{-1}$, the impact of GalC7 concentration on the color change position in the range from 0.22 mol.L^{-1} to 0.27 mol.L^{-1} is not significant (see SI-3). With lower HCl concentrations or higher injection rates the gel will not form during the fall. At higher HCl concentrations, the gel immediately forms a clog at the exit of the noddle. Finally, the microstructure of the gel has been observed by SEM (Fig. 4e). In these wet spinning conditions, with acid-base mixing, we

did not observe any specific organization of the supramolecular fibers. No radial organization nor organized spherulites have been seen.

2.3- Model

A simple model can be established to evaluate the position of the color switch point and how it changes as a function of the flow rate and the acid concentration. The model considers the moles of the base that have to be neutralized from the exit of the nozzle to the color change point. Since the molar ratio of NaOH to basic GalC7 is 32 and the molar ratio of NaOH to the pH indicator is 1600, (NaOH: 8 mol.L⁻¹; pH indicator: 5 μmol.L⁻¹; GalC7: 0.25 mol.L⁻¹) we approximate that the reaction of neutralization of OH⁻ is the main phenomenon at the origin of the pH changes in the jet. Also, in this model, [H⁺] is assumed to be constant (at the HCl concentration set experimentally), because the volume of the acid bath is much higher than the volume of the jet (the “reactor”).

The jet containing the bases (OH⁻, pH indicator and deprotonated GalC7) can be assumed to be a reactor that will react with the protons all around. The decrease of the concentration of base from the nozzle exit to the color switch point as a function of time, which is homogeneous to a reagent flow, ϕ , is given by equation (1), with d = distance of the color switch point in cm; $C_{OH}^0 = 8 \text{ mol.L}^{-1}$; C_{OH}^d = concentration of base at $\text{pH} = \text{pKa}$, i.e. $10^{-1} \text{ mol.L}^{-1}$ for acid fuchsin ($\text{pKa} = 13$), and $10^{-6} \text{ mol.L}^{-1}$ for phenol red ($\text{pKa} = 7.9$); t_d = time at which the color change occurs. If we also consider that the base reacts with the acid with a partial order of 1 for acid and for base, with k being the rate constant of the acid-base reaction then $\frac{d[OH^-]}{dt} = k[H^+][OH^-] = \phi$, then it comes:

Equation (1)

$$\phi = -\frac{C_{OH}^0 - C_{OH}^d}{0 - t_d} \approx k[H^+]C_{OH}^0$$

We now introduce a simplified geometry of the jet, which is considered as a tube of section S , with a flow of basic solution D (injection rate, μL/min). Thus, the volume of the basic solution between the nozzle exit and the color switch point is $S \cdot d$. The residence time of this volume in the acid solution is:

Equation (2)
$$t_d = \frac{S \cdot d}{D}$$

From equation (1), we obtain equation (3)
$$t_d = \frac{C_{OH}^0 - C_{OH}^d}{k[H^+]C_{OH}^0}$$

Combining equations (2) and (3) leads to equation (4), which gives the distance of the color change as a function of D and $[H^+]$:

Equation (4)
$$d = \frac{D}{S} \frac{C_{OH}^0 - C_{OH}^d}{k[H^+]C_{OH}^0} \approx \frac{D}{Sk[H^+]}$$

At $\text{pH} = \text{pKa}$, $C_{OH}^d = 10^{-1} \text{ mol.L}^{-1}$ for acid fuchsin and $10^{-6} \text{ mol.L}^{-1}$ for phenol red and $C_{OH}^0 = 8 \text{ mol.L}^{-1}$. Equation (4) is plotted in Figures 8a and b. In Figure 8a, D is set for each curve. In

Figure 8b, $[H^+]$ is set for each curve. Since $C_{OH}^d \ll C_{OH}^0$ there is no difference between the two indicators with this model when we plot the curves.

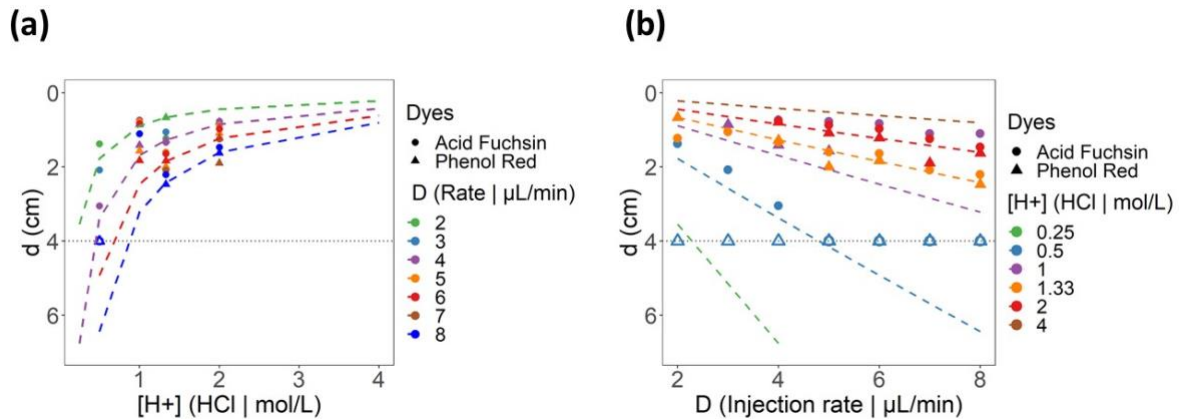


Fig.8: Model curves of the distance of neutralization of OH^- injected in a bath of H^+ (dotted lines). Means of the experimental color change points are represented in plain figures. Open figures represent conditions where the color change is not observed before the jet reaches the bottom of the vial (4 cm of fall: this limit is represented by the dotted line). In Fig 8a: D is set for each curve and $[H^+]$ varies on the X axis. In Figure 8b, $[H^+]$ is set for each curve and D varies on the X axis.

The model properly explains several tendencies observed in the experimental data.

1) The distance of color change increases linearly with the injection rate, for a given $[H^+]$ (Fig. 8b).

2) The slope of this linear relation increases when $[H^+]$ decreases in a non-linear fashion: The slope increases more as $[H^+]$ decreases, because d is proportional to $1/[H^+]$. This trend is clearly observed experimentally in Fig 7b for acid fuchsin.

3) As a result, the difference between the curves for HCl concentrations over 1M is low and stands within the experimental dispersion. It fits with the experimental results, where d changes slightly from 1 to 2M. (Fig 7a). In figure 7a and Fig 7b the curves are strongly distinct only when the concentration is 0.5M or below.

4) The model also shows the conditions where no color change occurs before reaching the bottom of the vial (4 cm). Again, it occurs for $HCl = 0.5$ M (and also at lower HCl concentration) and at flow rate above 5 $\mu\text{L}/\text{min}$.

5) The differences observed experimentally between the two indicators, especially for $[HCl] = 0.5$ mol.L $^{-1}$ are not explained by this model. Explaining this difference may require a more advanced model, such as a finer analysis of how $[OH^-]$ decreases along the jet. Also, other phenomena that are not taken in account are the effect of gravity, heat transfer, gel formation, turbulence, pump cycling etc. Despite these simplifications, the trends are properly described by the simplified model.

Finally, from the model curves, we extracted the constant k . The slopes of the affine lines of Fig. 8b give the value of $1/Sk$ for each $[H^+]$. The diameter of the jet measured from the snapshot of the video recordings is about 150 μm , with a constriction factor of 2.33, which enables to calculate a mean value of S . Then it gives $k = 0.2249 \pm 0.0093$ L/mol.s L.mol $^{-1}$.s $^{-1}$ (see SI-7). Since this reaction constant is far from the order of magnitude of the bimolecular reaction between H^+ and OH^- which is around 10^{11} L.mol $^{-1}$.s $^{-1}$ ⁶⁵, it means that this constant reflects

primarily the mixing rate and the limitation of the reactants in the system (HCl solution and NaOH solution).

2.4- 3D printing in acid-base aqueous conditions

In a previous work, we demonstrated that hydrogels from N-alkyl-D-galactonamides can be 3D-printed despite their mechanical fragility^{45,46}. The 3D printing was made by the injection of a solution of N-alkyl-D-galactonamide in DMSO, controlled by a drawing robot, in a bath of water (see SI-8). In the same way, we tested the printing of the GalC7 gel in only aqueous conditions, by acid-base exchange. An "F" pattern was used to evaluate the resolution and the shape fidelity of the print. It includes different spacings between the lines of the "F" (2 mm, 1 mm, 0.75 mm and 0.50 mm) and straight angles. The best conditions of printing used in DMSO/water exchange have been applied again (10 $\mu\text{L}/\text{min}$ and 4 mm/s; concentration of GalC7 is 0.23 mol.L⁻¹). It also gives a well-defined printed pattern. The concentration of GalC7 must be more than twice higher in acid-base conditions, as it is the case in wet spinning (68 mg/mL; 0.23 mol.L⁻¹). The width of the gel deposit has been measured to evaluate the resolution of the prints. Thinner gel deposits provided better resolution, as it reduces the possibility of gel deposits overlapping. Generally speaking, thin gel deposits are obtained if the gelation rate and/or if the ink viscosity are high, as the gel is formed before the spreading of the liquid ink. In the case of one-layered prints, we observed a better resolution in the case of the acid-base neutralization compared to the results obtained with the DMSO/water exchange approach. No overlapping of the gel deposits was observed, not even at the lowest spacing value, corresponding to 0.5 mm (Fig. 9a,b). The mean width of the gel deposits produced by the acid-base approach is 200 μm thinner than that of the previous approach (Table 2). This difference could be related to the fact that the viscosity of the GalC7 solution in NaOH 8 mol.L⁻¹ (GalC7 concentration: 0.2 mol.L⁻¹; viscosity: 2 Pa.s; 22°C) is 1000 times higher than the viscosity of the GalC7 solution in DMSO (GalC7 concentration: 25 mg/mL GalC7, 0.085 mol.L⁻¹; viscosity 3 mPa.s, 22°C). On a ten-layer print the shape fidelity was maintained. An overlapping of the gel was observed only at the lowest spacing value (Fig. 9c,d). Another noticeable change between the two approaches is the aspect of the gel deposit in one-layer print. Along the print, the gel's opacity is not constant. The center of the gel deposit is more transparent than the border. This observation recalls the formation of depletion zones observed in the precipitation of minerals (Liesegang rings) or supramolecular hydrogels¹⁶. The first GalC7 fibers nucleate at the border of the ink deposit, due to the neutralization by the acid solution. The fibers then grow from these nucleation points, draining the gelator molecules at the center of the liquid deposit. It results in a decrease of the concentration in gelator in the center. Such a phenomenon could explain the heterogeneity observed.

Mean width (mm)	Smallest width (mm)	Largest width (mm)	Injection rate ($\mu\text{L}/\text{min}$)	Printing speed (mm/s)	Approach
0.877	0.772	1.029	10	4	Acid-base (this paper)
1.081	0.952	1.231	10	4	Solvent exchange ⁽⁴⁵⁾

Table 2. Measurements of the gel deposits' width resulting from the two approaches

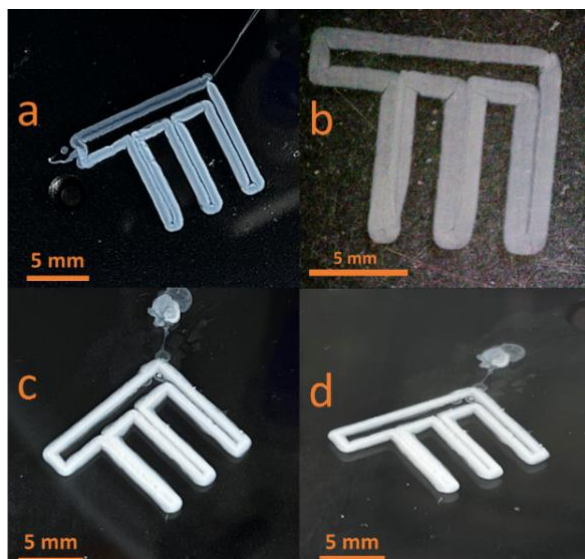


Fig. 9. 3D-printing of GalC7 (4 mm/s, 10 $\mu\text{L}/\text{min}$): (a) one layer in acid-base approach ($\text{HCl } 1 \text{ mol.L}^{-1}$); (b) one layer in DMSO/water exchange approach⁴⁵; (c-d) ten-layer print in acid-base approach ($\text{HCl } 2 \text{ mol.L}^{-1}$) top view (c) and perspective view (d).

Experimental section

N-hexyl-D-galactonamide, N-heptyl-D-galactonamide, N-octyl-D-galactonamide, N-nonyl-D-galactonamide have been synthesized according to the procedure described in ref.³⁴ or purchased from Innov'Orga (France). Dimethylsulfoxide (DMSO) with the quality: 99 % and non-anhydrous is used to dissolve the gelators (density: $1.0955 \text{ g}/\text{cm}^3$ at 25°C). Photos and videos were acquired with a DinoLite digital microscope (AM4013MTL-FVW) or a Canon EOS 600D under white light. The outer diameter of the needle (0.305 mm) is used to calibrate the images for measuring the filament diameters. ^1H NMR spectra have been recorded at 300 MHz (Bruker). Peaks have been assigned from 2D NMR homonuclear and heteronuclear coupling experiments (COSY, HSQC, HMBC) described in former publications³⁴.

Wet spinning in DMSO / water conditions

Solutions of N-hexyl-D-galactonamide, N-octyl-D-galactonamide, N-nonyl-D-galactonamide are prepared by dissolving the molecule at room temperature for 16 h in dimethyl sulfoxide at different mass concentrations according to graphics (from 10 to 100 mg/mL corresponding to 1 to 10 wt%). If needed, the sample is put in an ultrasound bath to help dissolution. The solutions are extruded in a bath of deionized water (50 mL, bath height: 5.7 cm) at room temperature ($21\text{-}23^\circ\text{C}$) with a syringe pump (Legato 111 from KD Scientific, vertical position). 50 mL polystyrene cell culture flasks are used as containers, since they have a high transparency and flat windows. It enables the acquisition of high-quality images and videos. Flow rates from 5 to 150 $\mu\text{L}/\text{min}$ are applied. Blunt tip needles of gauge 30G (internal diameter = 0.140 mm; outer diameter = 0.305 mm) are used. The end of the tip is immersed in water a few millimeters below the water/air interface, just before starting the injection. 50 μL of the solution are injected. 40 mL of water are removed just after injection, to reduce the volume of water and limit the dissolution of the filaments. The persistence of the filaments in this volume is observed after several days or months.

Stability of GalC7 in the basic medium

18 mg of GalC7 in thin powder was solubilized in 0.6 mL of sodium hydroxide 8 mol.L⁻¹. The solubilized gelator was left in NaOH for 5, 10, 30, and 60 min at room temperature. Then 1.2 mL of acetic acid 8 mol.L⁻¹ was added to neutralize the solution. The solution became milky-white upon the addition of acid. The formation of hydrogel was confirmed by putting the vial upside-down. The gel was lyophilized for at least 24 hours to remove water. Then 17 mg of the resulting white powder were dissolved in 0.5 mL of a mix of DMSO-d₆/D₂O (2.2 g DMSO-d₆ / 0.1 g D₂O), containing 16 mg of maleic acid as an internal standard (7 mmol.L⁻¹). The NMR spectrum is recorded and the presence of peaks corresponding to the alkylammonium (1.5 ppm for NH₃⁺-CH₂-CH₂- (quint.) and 2.7 ppm (t) for NH₃⁺-CH₂-) is controlled. A solution of GalC8 heated for 1h at 100°C shows around a 2/3 to 1/3 ratio of ammonium to the starting galactonamide, detected from these signals⁴⁵.

Wet spinning in acid-base conditions

GalC7 in thin powder was solubilized in sodium hydroxide (8 mol.L⁻¹) at room temperature at 0.25 mol.L⁻¹ ± 10% (73 ± 7 mg/mL), for 10 minutes without stirring. Wet spinning experiments are performed 15 to 45 minutes after the preparation of the samples. The following pH indicators were added to 1 mL of the NaOH solution when necessary, to visualize the pH changes during the formation of the gel filament: 1.7 mg (5 µmol/mL) of phenol red (pK_a = 7.9 from fuchsia basic form to yellow acidic form) or 1.5 mg (5 µmol/mL) of acid fuchsin (pK_a = 13, from colorless basic form to pink basic form) (5 mmol.L⁻¹). This gelator solution is then injected into a bath of 40 mL of hydrochloric acid, in 50 mL polystyrene culture flasks with flat transparent walls. The concentration of hydrochloric acid varied from 0.01 to 8 mol.L⁻¹. The solution was injected into the bath of acid at a rate varying from 2 to 8 µL/min, controlled by a syringe pump (Fusion 101R Chemyx). A 20G gauge blunt tip needle was used (internal diameter 600 µm, outer diameter 910 µm). The tip of the needle was submerged in the bath. The height of the fall (from the tip of the needle to the bottom of the flask) was 4 cm. Several pictures of the falling jet were taken. Close-up pictures were taken to visualize the precise point where the jet color had changed completely. The distance between that point of color change and the tip of the needle was measured. The distance was measured using ImageJ software. The results were plotted using the ggplot2 package in RStudio.

3D-printing in acid-base conditions

3D-printing was performed using a drawing/writing robot, Axidraw V3, coupled to a syringe pump from Chemyx Inc. (Model Fusion 100CR). The XY-axis movement of the robot is controlled by the software Inkscape. The Z-axis is changed manually by using a Z-moving platform. "F"-patterns were printed in 8 cm diameter polystyrene Petri dishes. The Petri dishes were filled with 25 mL of concentrated aqueous solution of hydrochloric acid. The syringe filled with the gelator solution was adapted to the syringe pump and connected to the Axidraw pen holder with tubing and luer-lock needle adapters. The GalC7 solutions (68 mg/mL; 0.23 mol.L⁻¹) were extruded in the acid bath (HCl 2 mol.L⁻¹) through blunt tip 30G needles (ID 160 µm). The distance between the tip and the drawing surface was set at 300 µm.

Cryo-SEM observations

Gel filaments prepared by wet spinning were retrieved with a sieve placed in the coagulation bath. A part of the gel filament is deposited on the cryo-SEM cane and frozen at -220 °C in a liquid nitrogen slush. The frozen sample was fractured at -145 °C under vacuum in the cryo-transfer system chamber (Quorum PP3000T). The freeze-drying was performed at -95 °C for 1h. The sample was metalized with Pd for 60 s and introduced in the microscope. The

temperature was kept at $-145\text{ }^{\circ}\text{C}$. Images were recorded with a FEG FEI Quanta 250 microscope, at 5 kV for the acceleration voltage.

Rheology

Viscosity of the solutions have been measured with a rheometer AR1000 (TA) equipped with a stainless steel cone plate configuration (6 cm, 2°) and measured at a shear rate of 10 s^{-1} at 22°C .

Conclusion

In this work, we have shown that N-alkyl-D-galactonamides can be wet spun in different conditions, either by DMSO-water switch or by acido-basic switch. The wet spinning can be performed in only aqueous conditions thanks to the solubilization of N-alkyl-D-galactonamides in concentrated basic solution ($\text{NaOH } 8\text{ mol.L}^{-1}$). In both conditions, a well-shaped continuous jet falls vertically in the water bath, thanks to the difference in density. The self-assembly of the gelator is progressively triggered by the decrease of its solubility in contact with water. When the concentrations and injection rates are adjusted properly to avoid clogs or too late a gelation, a filament of gel forms during the fall, leading to the formation of well-shaped gel coils. In acid-base conditions, the jet is more unstable compared with DMSO-water conditions. In DMSO-water conditions, typical concentrations for short chain N-hexyl-D-galactonamide and N-heptyl-D-galactonamide³⁶ is 40 mg/mL at an injection rate of $10\text{-}20\text{ }\mu\text{L/min}$, while typical concentrations for long-chain N-octyl and N-nonyl-D-galactonamides is $10\text{-}30\text{ mg/mL}$ at an injection rate of $50\text{ }\mu\text{L/min}$. In acid-base conditions, the neutralization of the base solution charged with N-alkylgalactonamide lead to a gel filament when HCl concentration is high enough (above 1 mol.L^{-1}) and for injection rates comprised between 2 and $8\text{ }\mu\text{L/min}$ and a concentration of N-heptyl-D-galactonamide from 65 to 80 mg/mL . The progressive acid/base neutralization along the jet is related to the injection rate and has been very well observed thanks to the addition of two pH indicators, phenol red and acid fuchsin. A simplified theoretical model was able to explain the main experimental observations. The acid-base exchange has also been applied successfully to 3D printing, giving well-resolved patterns.

This “all-aqueous” wet spinning method paves the way to spinning mineral species such as metal hydroxides⁵⁶, calcium phosphate⁵⁷ or polyoxometalates⁶⁶⁻⁶⁹, through supramolecular interactions with the gelator. A specific organization of these species during the spinning process, induced by the gelator self-assembly and interfacial phenomena is expected. This technique is also interesting for injecting other non-thixotropic hydrogels and can be further adapted to 3D printing and spatially controlled gelation^{45,46,70,71}.

Acknowledgements

Bruno Payré and Dominique Goudounèche (CMEAB “Centre de Microscopie Electronique Appliqué à la Biologie”, Toulouse) are acknowledged for their assistance in the acquisition of electronic microscopy images. We thank Caroline Toppan (NMR) of the Institut de Chimie de Toulouse ICT-FR 2599 for NMR facilities (Université de Toulouse, CNRS, Toulouse, France, <https://ict.cnrs.fr>). Delphine Bordignon is acknowledged for the synthesis of N-alkyl-D-galactonamide samples. This work was supported by the French Ministry of Higher Education, Research and Innovation (Ministère de l'Enseignement Supérieur, de la Recherche et de l'Innovation) for F.A.'s grant, L'Ecole Nationale Vétérinaire de Toulouse, ENVT for Salomé

Peters Internship and the French National Research Agency (ANR “Neuraxe”, grant N°ANR-15-CE07-0007-01).

References

- (1) Du, X.; Zhou, J.; Shi, J.; Xu, B. Supramolecular Hydrogelators and Hydrogels: From Soft Matter to Molecular Biomaterials. *Chem. Rev.* **2015**, *115* (24), 13165–13307. <https://doi.org/10.1021/acs.chemrev.5b00299>.
- (2) Zhang, J.; Hu, Y.; Li, Y. Supramolecular Gels. In *Gel Chemistry: Interactions, Structures and Properties*; Zhang, J., Hu, Y., Li, Y., Eds.; Lecture Notes in Chemistry; Springer: Singapore, 2018; pp 9–59. https://doi.org/10.1007/978-981-10-6881-2_2.
- (3) Shao, T.; Falcone, N.; Kraatz, H.-B. Supramolecular Peptide Gels: Influencing Properties by Metal Ion Coordination and Their Wide-Ranging Applications. *ACS Omega* **2020**, *5* (3), 1312–1317. <https://doi.org/10.1021/acsomega.9b03939>.
- (4) Eelkema, R.; Pich, A. Pros and Cons: Supramolecular or Macromolecular: What Is Best for Functional Hydrogels with Advanced Properties? *Advanced Materials* **2020**, *32* (20), 1906012. <https://doi.org/10.1002/adma.201906012>.
- (5) Wu, H.; Zheng, J.; Kjøniksen, A.-L.; Wang, W.; Zhang, Y.; Ma, J. Metallogels: Availability, Applicability, and Advanceability. *Advanced Materials* **2019**, *31* (12), 1806204. <https://doi.org/10.1002/adma.201806204>.
- (6) Draper, E. R.; Adams, D. J. Low-Molecular-Weight Gels: The State of the Art. *Chem* **2017**, *3* (3), 390–410. <https://doi.org/10.1016/j.chempr.2017.07.012>.
- (7) Morris, J.; Bietsch, J.; Bashaw, K.; Wang, G. Recently Developed Carbohydrate Based Gelators and Their Applications. *Gels* **2021**, *7* (1), 24. <https://doi.org/10.3390/gels7010024>.
- (8) Criado-Gonzalez, M.; Wagner, D.; Iqbal, M. H.; Ontani, A.; Carvalho, A.; Schmutz, M.; Schlenoff, J. B.; Schaaf, P.; Jierry, L.; Boulmedais, F. Supramolecular Tripeptide Self-Assembly Initiated at the Surface of Coacervates by Polyelectrolyte Exchange. *Journal of Colloid and Interface Science* **2021**, *588*, 580–588. <https://doi.org/10.1016/j.jcis.2020.12.066>.
- (9) Holey, S. A.; Sekhar, K. P. C.; Swain, D. K.; Bojja, S.; Nayak, R. R. Supramolecular Glycolipid-Based Hydro-/Organogels with Enzymatic Bioactive Release Ability by Tuning the Chain Length and Headgroup Size. *ACS Biomater. Sci. Eng.* **2022**, *8* (3), 1103–1114. <https://doi.org/10.1021/acsbomaterials.1c01510>.
- (10) Benizri, S.; Gaubert, A.; Soulard, C.; Gontier, É.; Svahn, I.; Rocchi, P.; Vacher, G.; Barthélémy, P. Hydrogel Based Lipid-Oligonucleotides: A New Route to Self-Delivery of Therapeutic Sequences. *Biomater. Sci.* **2021**, *9* (10), 3638–3644. <https://doi.org/10.1039/D1BM00273B>.
- (11) Sindhu, K. R.; Bansode, N.; Rémy, M.; Morel, C.; Bareille, R.; Hagedorn, M.; Hinz, B.; Barthélémy, P.; Chassande, O.; Boiziau, C. New Injectable Self-Assembled Hydrogels That Promote Angiogenesis through a Bioactive Degradation Product. *Acta Biomaterialia* **2020**, *115*, 197–209. <https://doi.org/10.1016/j.actbio.2020.08.012>.
- (12) Rangel Euzcateguy, G.; Parajua-Sejil, C.; Marchal, P.; Chapron, D.; Averlant-Petit, M.-C.; Stefan, L.; Pickaert, G.; Durand, A. Rheological Investigation of the Influence of Dextran on the Self-Assembly of Lysine Derivatives in Water/Dimethylsulfoxide Mixtures. *Colloids and Surfaces A: Physicochemical and Engineering Aspects* **2021**, *625*, 126908. <https://doi.org/10.1016/j.colsurfa.2021.126908>.
- (13) Giraud, T.; Bouguet-Bonnet, S.; Marchal, P.; Pickaert, G.; Averlant-Petit, M.-C.; Stefan, L. Improving and Fine-Tuning the Properties of Peptide-Based Hydrogels via Incorporation of Peptide Nucleic Acids. *Nanoscale* **2020**, *12* (38), 19905–19917. <https://doi.org/10.1039/D0NR03483E>.
- (14) Messaoud, G. B.; Griel, P. L.; Hermida-Merino, D.; Baccile, N. Effects of PH, Temperature and Shear on the Structure–Property Relationship of Lamellar Hydrogels from Microbial

- Glucolipids Probed by in Situ Rheo-SAXS. *Soft Matter* **2020**, *16* (10), 2540–2551. <https://doi.org/10.1039/C9SM02494H>.
- (15) Baccile, N.; Ben Messaoud, G.; Le Griel, P.; Cowieson, N.; Perez, J.; Geys, R.; De Graeve, M.; Roelants, S. L. K. W.; Soetaert, W. Palmitic Acid Sophorolipid Biosurfactant: From Self-Assembled Fibrillar Network (SAFiN) to Hydrogels with Fast Recovery. *Philosophical Transactions of the Royal Society A: Mathematical, Physical and Engineering Sciences* **2021**, *379* (2206), 20200343. <https://doi.org/10.1098/rsta.2020.0343>.
- (16) Runser, J.-Y.; Criado-Gonzalez, M.; Fneich, F.; Rabineau, M.; Senger, B.; Weiss, P.; Jierry, L.; Schaaf, P. Non-Monotonous Enzyme-Assisted Self-Assembly Profiles Resulting from Reaction-Diffusion Processes in Host Gels. *Journal of Colloid and Interface Science* **2022**, *620*, 234–241. <https://doi.org/10.1016/j.jcis.2022.03.150>.
- (17) Adams, D. J. Personal Perspective on Understanding Low Molecular Weight Gels. *J. Am. Chem. Soc.* **2022**, *144* (25), 11047–11053. <https://doi.org/10.1021/jacs.2c02096>.
- (18) Ono, F.; Ichimaru, K.; Hirata, O.; Shinkai, S.; Watanabe, H. Universal Glucose-Based Low-Molecular-Weight Gelators for Both Organic and Aqueous Solvents. *Chem. Lett.* **2019**, *49* (2), 156–159. <https://doi.org/10.1246/cl.190769>.
- (19) Higashi, S. L.; Ikeda, M. Development of an Amino Sugar-Based Supramolecular Hydrogelator with Reduction Responsiveness. *JACS Au* **2021**, *1* (10), 1639–1646. <https://doi.org/10.1021/jacsau.1c00270>.
- (20) Barclay, T. G.; Constantopoulos, K.; Matisons, J. Nanotubes Self-Assembled from Amphiphilic Molecules via Helical Intermediates. *Chemical Reviews* **2014**, *114* (20), 10217–10291. <https://doi.org/10.1021/cr400085m>.
- (21) Matthews, L.; Przybyłowicz, Ż.; Rogers, S. E.; Bartlett, P.; Johnson, A. J.; Sochon, R.; Briscoe, W. H. The Curious Case of SDS Self-Assembly in Glycerol: Formation of a Lamellar Gel. *Journal of Colloid and Interface Science* **2020**, *572*, 384–395. <https://doi.org/10.1016/j.jcis.2020.03.102>.
- (22) Arokianathan, J. F.; Ramya, K. A.; Deshpande, A. P.; Leemarose, A.; Shanmugam, G. Supramolecular Organogel Based on Di-Fmoc Functionalized Unnatural Amino Acid: An Attempt to Develop a Correlation between Molecular Structure and Ambidextrous Gelation. *Colloids and Surfaces A: Physicochemical and Engineering Aspects* **2021**, *618*, 126430. <https://doi.org/10.1016/j.colsurfa.2021.126430>.
- (23) Ibrahim, M. I. A.; Pickaert, G.; Stefan, L.; Jamart-Grégoire, B.; Bodiguel, J.; Averlant-Petit, M.-C. Cyclohexamer [-(D-Phe-AzaPhe-Ala)₂-]: Good Candidate to Formulate Supramolecular Organogels. *RSC Adv.* **2020**, *10* (71), 43859–43869. <https://doi.org/10.1039/D0RA07775E>.
- (24) Salazar-Bautista, S.-C.; Chebil, A.; Pickaert, G.; Gaucher, C.; Jamart-Gregoire, B.; Durand, A.; Leonard, M. Encapsulation and Release of Hydrophobic Molecules from Particles of Gelled Triglyceride with Aminoacid-Based Low-Molecular Weight Gelators. *Colloids and Surfaces A: Physicochemical and Engineering Aspects* **2017**, *514*, 11–20. <https://doi.org/10.1016/j.colsurfa.2016.11.045>.
- (25) Gao, J.; Okazaki, Y.; Pouget, E.; Nlate, S.; Kauffmann, B.; Artzner, F.; Buffeteau, T.; Oda, R. Slow Kinetic Evolution of Nanohelices Based on Gemini Surfactant Self-Assemblies with Various Enantiomeric Excess; Chiral Segregation towards a Racemic Mixture. *Mater. Chem. Front.* **2021**, *5* (7), 3021–3028. <https://doi.org/10.1039/D0QM00989J>.
- (26) Jierry, L. Non-Monotonous Enzyme-Assisted Self-Assembly Profiles Resulting from Reaction-Diffusion Processes in Host Gels. **2022**.
- (27) Yao, S.; Brahmi, R.; Bouschon, A.; Chen, J.; Halila, S. Supramolecular Carbohydrate-Based Hydrogels from Oxidative Hydroxylation of Amphiphilic β -C-Glycosylbarbiturates and α -Glucosidase-Induced Hydrogelation. *Green Chem.* **2022**. <https://doi.org/10.1039/D2GC04180D>.
- (28) Clemente, M. J.; Tejedor, R. M.; Romero, P.; Fitremann, J.; Oriol, L. Maltose-Based Gelators Having Azobenzene as Light-Sensitive Unit. *RSC Advances* **2012**, *2* (30), 11419. <https://doi.org/10.1039/c2ra21506c>.

- (29) Wang, Y.; de Kruijff, R. M.; Lovrak, M.; Guo, X.; Eelkema, R.; van Esch, J. H. Access to Metastable Gel States Using Seeded Self-Assembly of Low-Molecular-Weight Gelators. *Angewandte Chemie International Edition* **2019**, *58* (12), 3800–3803. <https://doi.org/10.1002/anie.201812412>.
- (30) Lovrak, M.; Hendriksen, W. E.; Kreutzer, M. T.; Steijn, V. van; Eelkema, R.; Esch, J. H. van. Control over the Formation of Supramolecular Material Objects Using Reaction–Diffusion. *Soft Matter* **2019**, *15* (21), 4276–4283. <https://doi.org/10.1039/C8SM02588F>.
- (31) Criado-Gonzalez, M.; Runser, J.-Y.; Carvalho, A.; Boulmedais, F.; Weiss, P.; Schaaf, P.; Jierry, L. Enzymatically-Active Nanoparticles to Direct the Self-Assembly of Peptides in Hydrogel with a 3D Spatial Control. *Polymer* **2022**, *261*, 125398. <https://doi.org/10.1016/j.polymer.2022.125398>.
- (32) Huang, X.; Raghavan, S. R.; Terech, P.; Weiss, R. G. Distinct Kinetic Pathways Generate Organogel Networks with Contrasting Fractality and Thixotropic Properties. *Journal of the American Chemical Society* **2006**, *128* (47), 15341–15352. <https://doi.org/10.1021/ja0657206>.
- (33) Lan, Y.; Corradini, M. G.; Liu, X.; May, T. E.; Borondics, F.; Weiss, R. G.; Rogers, M. A. Comparing and Correlating Solubility Parameters Governing the Self-Assembly of Molecular Gels Using 1,3:2,4-Dibenzylidene Sorbitol as the Gelator. *Langmuir* **2014**, *30* (47), 14128–14142. <https://doi.org/10.1021/la5008389>.
- (34) Chalard, A.; Vaysse, L.; Joseph, P.; Malaquin, L.; Souleille, S.; Lonetti, B.; Sol, J.-C.; Loubinoux, I.; Fitremann, J. Simple Synthetic Molecular Hydrogels from Self-Assembling Alkylgalactonamides as Scaffold for 3D Neuronal Cell Growth. *ACS Appl. Mater. Interfaces* **2018**, *10* (20), 17004–17017. <https://doi.org/10.1021/acsami.8b01365>.
- (35) Yamaguchi, D.; Ikemoto, Y.; Kato, T. Thermally Tunable Selective Formation of Self-Assembled Fibers into Two Orthogonal Directions in Oriented Liquid-Crystalline Smectic Templates. *Chem. Commun.* **2020**, *56* (69), 9954–9957. <https://doi.org/10.1039/D0CC01950J>.
- (36) Chalard, A.; Joseph, P.; Souleille, S.; Lonetti, B.; Saffon-Merceron, N.; Loubinoux, I.; Vaysse, L.; Malaquin, L.; Fitremann, J. Wet Spinning and Radial Self-Assembly of a Carbohydrate Low Molecular Weight Gelator into Well Organized Hydrogel Filaments. *Nanoscale* **2019**, *11* (32), 15043–15056. <https://doi.org/10.1039/C9NR02727K>.
- (37) Schlichter, L.; Piras, C. C.; Smith, D. K. Spatial and Temporal Diffusion-Control of Dynamic Multi-Domain Self-Assembled Gels. *Chem. Sci.* **2021**, *12* (11), 4162–4172. <https://doi.org/10.1039/D0SC06862D>.
- (38) Panja, S.; Adams, D. J. Stimuli Responsive Dynamic Transformations in Supramolecular Gels. *Chem. Soc. Rev.* **2021**, *50* (8), 5165–5200. <https://doi.org/10.1039/D0CS01166E>.
- (39) Bayram, K. K.; Fitremann, J.; Bayram, A.; Yılmaz, Z.; Mehmetbeyoğlu, E.; Özkul, Y.; Rassoulzadegan, M. Gene Expression of Mouse Hippocampal Stem Cells Grown in a Galactose-Derived Molecular Gel Compared to In Vivo and Neurospheres. *Processes* **2021**, *9* (4), 716. <https://doi.org/10.3390/pr9040716>.
- (40) Piras, C. C.; Mahon, C. S.; Genever, P. G.; Smith, D. K. Shaping and Patterning Supramolecular Materials–Stem Cell-Compatible Dual-Network Hybrid Gels Loaded with Silver Nanoparticles. *ACS Biomater. Sci. Eng.* **2022**, *8* (5), 1829–1840. <https://doi.org/10.1021/acsbiomaterials.1c01560>.
- (41) Zhan, H.; Löwik, D. W. P. M. A Hybrid Peptide Amphiphile Fiber PEG Hydrogel Matrix for 3D Cell Culture. *Advanced Functional Materials* **2019**, *29* (16), 1808505. <https://doi.org/10.1002/adfm.201808505>.
- (42) Rauf, S.; Susapto, H. H.; Kahin, K.; Alshehri, S.; Abdelrahman, S.; Lam, J. H.; Asad, S.; Jadhav, S.; Sundaramurthi, D.; Gao, X.; Hauser, C. A. E. Self-Assembling Tetrameric Peptides Allow in Situ 3D Bioprinting under Physiological Conditions. *J. Mater. Chem. B* **2021**, *9* (4), 1069–1081. <https://doi.org/10.1039/D0TB02424D>.
- (43) Marchini, A.; Favoino, C.; Gelain, F. Multi-Functionalized Self-Assembling Peptides as Reproducible 3D Cell Culture Systems Enabling Differentiation and Survival of Various Human Neural Stem Cell Lines. *Frontiers in Neuroscience* **2020**, *14*.

- (44) Godbe, J. M.; Freeman, R.; Burbulla, L. F.; Lewis, J.; Krainc, D.; Stupp, S. I. Gelator Length Precisely Tunes Supramolecular Hydrogel Stiffness and Neuronal Phenotype in 3D Culture. *ACS Biomater. Sci. Eng.* **2020**, *6* (2), 1196–1207. <https://doi.org/10.1021/acsbomaterials.9b01585>.
- (45) Andriamiseza, F.; Bordignon, D.; Payré, B.; Vaysse, L.; Fitremann, J. 3D Printing of Biocompatible Low Molecular Weight Gels: Imbricated Structures with Sacrificial and Persistent N-Alkyl-d-Galactonamides. *Journal of Colloid and Interface Science* **2022**, *617*, 156–170. <https://doi.org/10.1016/j.jcis.2022.02.076>.
- (46) Chalard, A.; Mauduit, M.; Souleille, S.; Joseph, P.; Malaquin, L.; Fitremann, J. 3D Printing of a Biocompatible Low Molecular Weight Supramolecular Hydrogel by Dimethylsulfoxide Water Solvent Exchange. *Additive Manufacturing* **2020**, *33*, 101162. <https://doi.org/10.1016/j.addma.2020.101162>.
- (47) Okesola, B. O.; Mendoza-Martinez, A. K.; Cidonio, G.; Derkus, B.; Boccorh, D. K.; Osuna de la Peña, D.; Elsharkawy, S.; Wu, Y.; Dawson, J. I.; Wark, A. W.; Knani, D.; Adams, D. J.; Oreffo, R. O. C.; Mata, A. De Novo Design of Functional Coassembling Organic–Inorganic Hydrogels for Hierarchical Mineralization and Neovascularization. *ACS Nano* **2021**, *15* (7), 11202–11217. <https://doi.org/10.1021/acsnano.0c09814>.
- (48) Jung, J. H.; Lee, S. S.; Shinkai, S.; Iwaura, R.; Shimizu, T. Novel Silica Nanotubes Using a Library of Carbohydrate Gel Assemblies as Templates for Sol-Gel Transcription in Binary Systems. *6*.
- (49) Panja, S.; Adams, D. J. Mimicking Evolution of ‘Mini-Homeostatic’ Modules in Supramolecular Systems. *Giant* **2020**, 100041. <https://doi.org/10.1016/j.giant.2020.100041>.
- (50) Bordignon, D.; Lonetti, B.; Coudret, C.; Roblin, P.; Joseph, P.; Malaquin, L.; Chalard, A.; Fitremann, J. Wet Spinning of a Library of Carbohydrate Low Molecular Weight Gels. *Journal of Colloid and Interface Science* **2021**, *603*, 333–343. <https://doi.org/10.1016/j.jcis.2021.06.058>.
- (51) Piras, C. C.; Kay, A. G.; Genever, P. G.; Fitremann, J.; Smith, D. K. Self-Assembled Gel Tubes, Filaments and 3D-Printing with in Situ Metal Nanoparticle Formation and Enhanced Stem Cell Growth. *Chem. Sci.* **2022**, *13* (7), 1972–1981. <https://doi.org/10.1039/D1SC06062G>.
- (52) Drew, E. N.; Piras, C. C.; Fitremann, J.; Smith, D. K. Wet-Spinning Multi-Component Low-Molecular-Weight Gelators to Print Synergistic Soft Materials. *Chem. Commun.* **2022**, *58* (79), 11115–11118. <https://doi.org/10.1039/D2CC04003D>.
- (53) Fuhrhop, J. H.; Schnieder, P.; Boekema, E.; Helfrich, W. Lipid Bilayer Fibers from Diastereomeric and Enantiomeric N-Octylaldonamides. *Journal of the American Chemical Society* **1988**, *110* (9), 2861–2867.
- (54) Pfannemüller, B.; Welte, W. Amphiphilic Properties of Synthetic Glycolipids Based on Amide Linkages. I. Electron Microscopic Studies on Aqueous Gels. *Chemistry and Physics of Lipids* **1985**, *37* (3), 227–240. [https://doi.org/10.1016/0009-3084\(85\)90011-8](https://doi.org/10.1016/0009-3084(85)90011-8).
- (55) Barge, L. M.; Cardoso, S. S. S.; Cartwright, J. H. E.; Cooper, G. J. T.; Cronin, L.; De Wit, A.; Doloboff, I. J.; Escribano, B.; Goldstein, R. E.; Haudin, F.; Jones, D. E. H.; Mackay, A. L.; Maselko, J.; Pagano, J. J.; Pantaleone, J.; Russell, M. J.; Sainz-Díaz, C. I.; Steinbock, O.; Stone, D. A.; Tanimoto, Y.; Thomas, N. L. From Chemical Gardens to Chemobionics. *Chem. Rev.* **2015**, *115* (16), 8652–8703. <https://doi.org/10.1021/acs.chemrev.5b00014>.
- (56) Barge, L. M.; Abedian, Y.; Russell, M. J.; Doloboff, I. J.; Cartwright, J. H. E.; Kidd, R. D.; Kanik, I. From Chemical Gardens to Fuel Cells: Generation of Electrical Potential and Current Across Self-Assembling Iron Mineral Membranes. *Angewandte Chemie International Edition* **2015**, *54* (28), 8184–8187. <https://doi.org/10.1002/anie.201501663>.
- (57) Hughes, E. A. B.; Chipara, M.; Hall, T. J.; Williams, R. L.; Grover, L. M. Chemobionic Structures in Tissue Engineering: Self-Assembling Calcium Phosphate Tubes as Cellular Scaffolds. *Biomater. Sci.* **2020**, *8* (3), 812–822. <https://doi.org/10.1039/C9BM01010F>.
- (58) Haase, M. F.; Jeon, H.; Hough, N.; Kim, J. H.; Stebe, K. J.; Lee, D. Multifunctional Nanocomposite Hollow Fiber Membranes by Solvent Transfer Induced Phase Separation. *Nat Commun* **2017**, *8* (1), 1234. <https://doi.org/10.1038/s41467-017-01409-3>.

- (59) Enache, A. A.; David, L.; Puaux, J.-P.; Banu, I.; Bozga, G. Kinetics of Chitosan Coagulation from Aqueous Solutions. *Journal of Applied Polymer Science* **2018**, *135* (16), 46062. <https://doi.org/10.1002/app.46062>.
- (60) Kumar, P.; Sebők, D.; Kukovecz, Á.; Horváth, D.; Tóth, Á. Hierarchical Self-Assembly of Metal-Ion-Modulated Chitosan Tubules. *Langmuir* **2021**, *37* (43), 12690–12696. <https://doi.org/10.1021/acs.langmuir.1c02097>.
- (61) Appendix 2: Dissociation Constants (PKa) of Common Sugars and Alcohols. In *Applications of Ion Chromatography for Pharmaceutical and Biological Products*; John Wiley & Sons, Ltd, 2012; pp 455–456. <https://doi.org/10.1002/9781118147009.app2>.
- (62) Pótári, G.; Tóth, Á.; Horváth, D. Precipitation Patterns Driven by Gravity Current. *Chaos* **2019**, *29* (7), 073117. <https://doi.org/10.1063/1.5094491>.
- (63) Tóth-Szeles, E.; Bohner, B.; Tóth, Á.; Horváth, D. Spatial Separation of Copper and Cobalt Oxalate by Flow-Driven Precipitation. *Cryst. Growth Des.* **2017**, *6*.
- (64) Ramachandran, R. Fingering versus Stability in the Limit of Zero Interfacial Tension. *NATURE COMMUNICATIONS* **2014**, *6*.
- (65) Eigen, M. Proton Transfer, Acid-Base Catalysis, and Enzymatic Hydrolysis. Part I: ELEMENTARY PROCESSES. *Angewandte Chemie International Edition in English* **1964**, *3* (1), 1–19. <https://doi.org/10.1002/anie.196400011>.
- (66) Li, B.; Xuan, L.; Wu, L. Polyoxometalate-Containing Supramolecular Gels. *Macromolecular Rapid Communications* **2022**, 2200019. <https://doi.org/10.1002/marc.202200019>.
- (67) Sun, N.; Wu, A.; Yu, Y.; Gao, X.; Zheng, L. Polyoxometalate-Based Photochromic Supramolecular Hydrogels with Highly Ordered Spherical and Cylindrical Micellar Nanostructures. *Chemistry – A European Journal* **2019**, *25* (24), 6203–6211. <https://doi.org/10.1002/chem.201900478>.
- (68) Zhang, G.; Zhang, J.; Wang, Y.; Wu, Y.; Li, Q.; Liang, Y.; Qi, W.; Rao, H.; Su, R.; He, Z. Self-Assembly of Multifunctional Hydrogels with Polyoxometalates Helical Arrays Using Nematic Peptide Liquid Crystal Template. *Journal of Colloid and Interface Science* **2020**, *578*, 218–228. <https://doi.org/10.1016/j.jcis.2020.05.116>.
- (69) Schmid, P. Self-Assembly of a Short Amphiphile in Water Controlled by Superchaotropic Polyoxometalates: H₄SiW₁₂O₄₀ vs. H₃PW₁₂O₄₀. *Journal of Colloid and Interface Science* **2021**, *11*.
- (70) Piras, C. C.; Mahon, C. S.; Genever, P.; Smith, D. K. Shaping and Patterning. *ACS Biomaterials Science & Engineering* **2022**.
- (71) Zhang, R.; Deng, L.; Guo, J.; Yang, H.; Zhang, L.; Cao, X.; Yu, A.; Duan, B. Solvent Mediating the in Situ Self-Assembly of Polysaccharides for 3D Printing Biomimetic Tissue Scaffolds. *ACS Nano* **2021**, *15* (11), 17790–17803. <https://doi.org/10.1021/acsnano.1c05956>.

Supplementary material

Wet spinning and 3D printing of supramolecular hydrogels in acid-base and dynamic conditions

Faniry Andriamiseza^{§,1}, Salomé Peters^{§,1}, Clément Roux¹, Nicolas Dietrich², Christophe Coudret¹, Juliette Fitremann^{*,1}

¹ Laboratoire des IMRCP, Université de Toulouse, CNRS UMR 5623, Université Toulouse III - Paul Sabatier, Toulouse, France

² Toulouse Biotechnology Institute, Université de Toulouse, CNRS, INRAE, INSA, Toulouse, France

SI-1- Microstructure of the gel filaments in DMSO/water wet spinning conditions

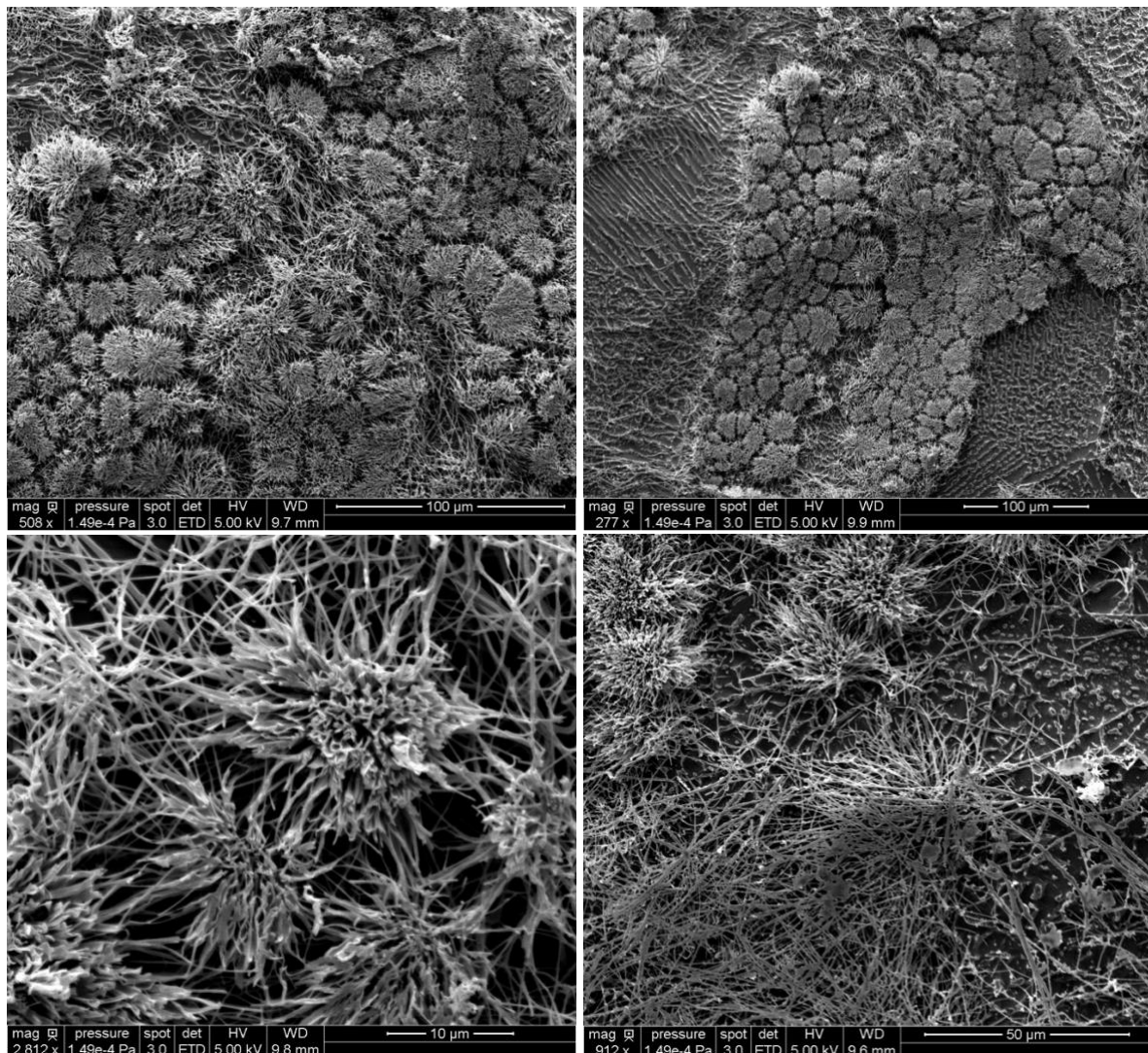


Fig. SI-1.1. *N*-hexyl-*D*-galactonamide, GalC6 100 mg/mL; 20 μL/min

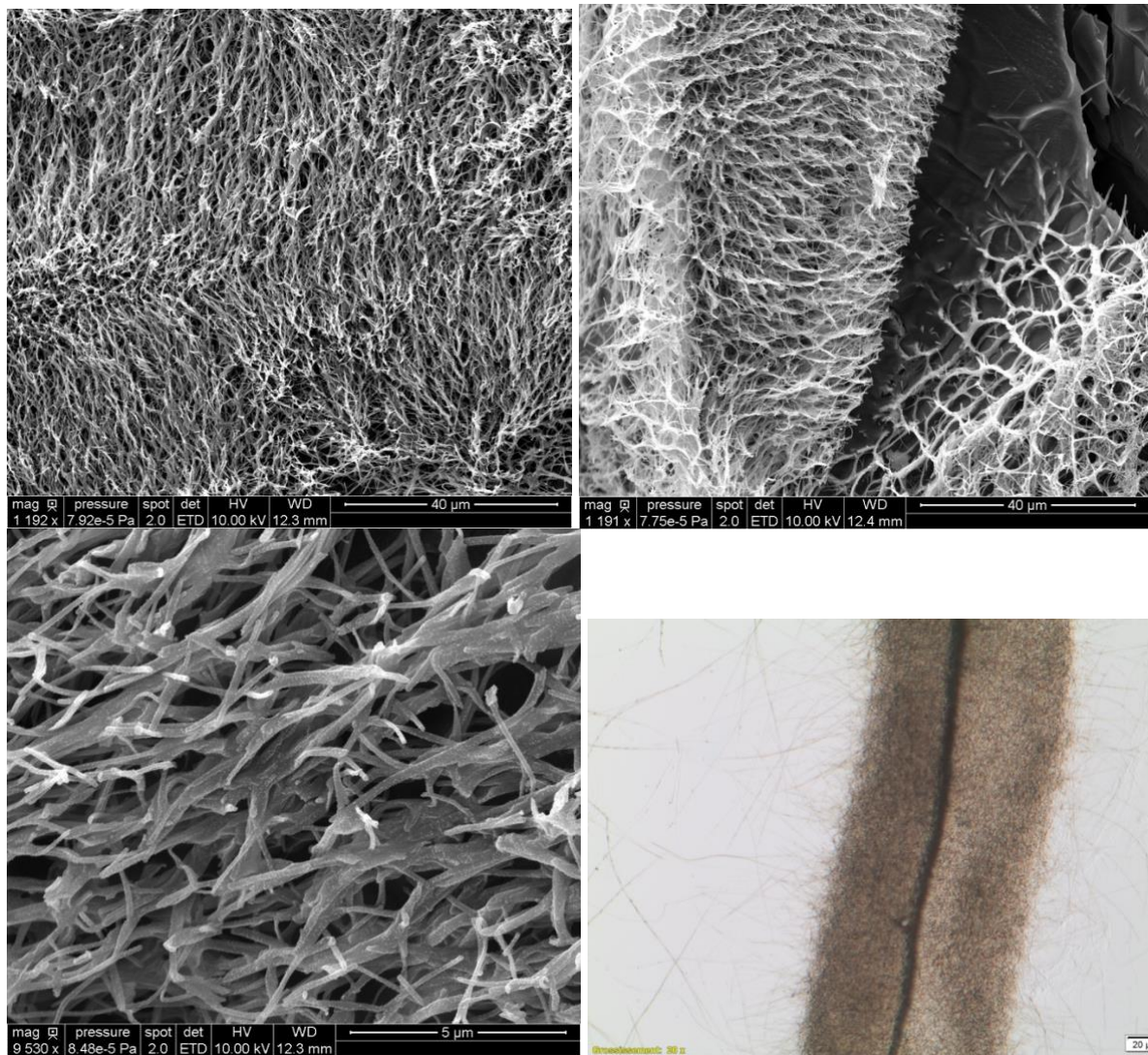


Fig. SI-1.2. *N*-octyl-*D*-galactonamide, GalC8 25 mg/mL ; 25 μ L/min

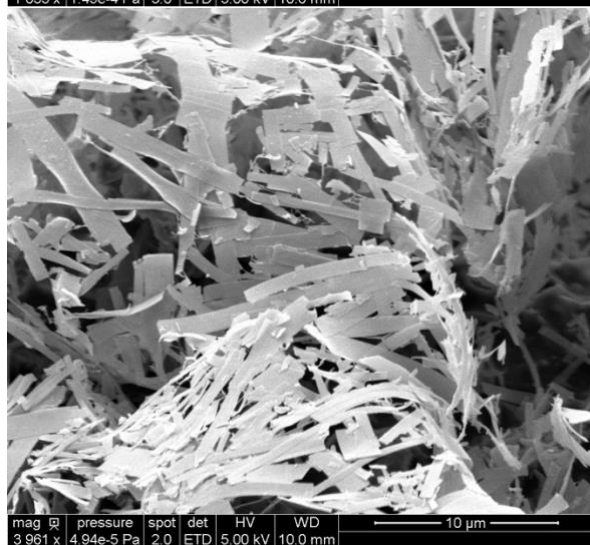
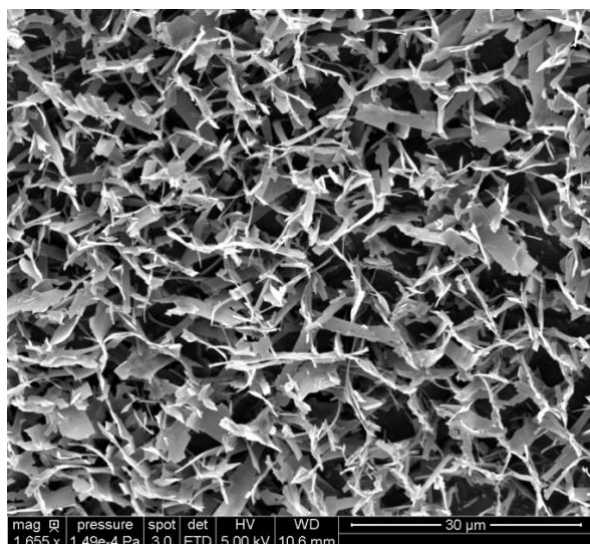


Fig. SI-1.3. *N*-nonyl-*D*-galactonamide, GalC9 10 mg/mL; 20 μL/min

SI-2- NMR spectra of N-heptyl-D-galactonamide in NaOH 8 mol.L⁻¹

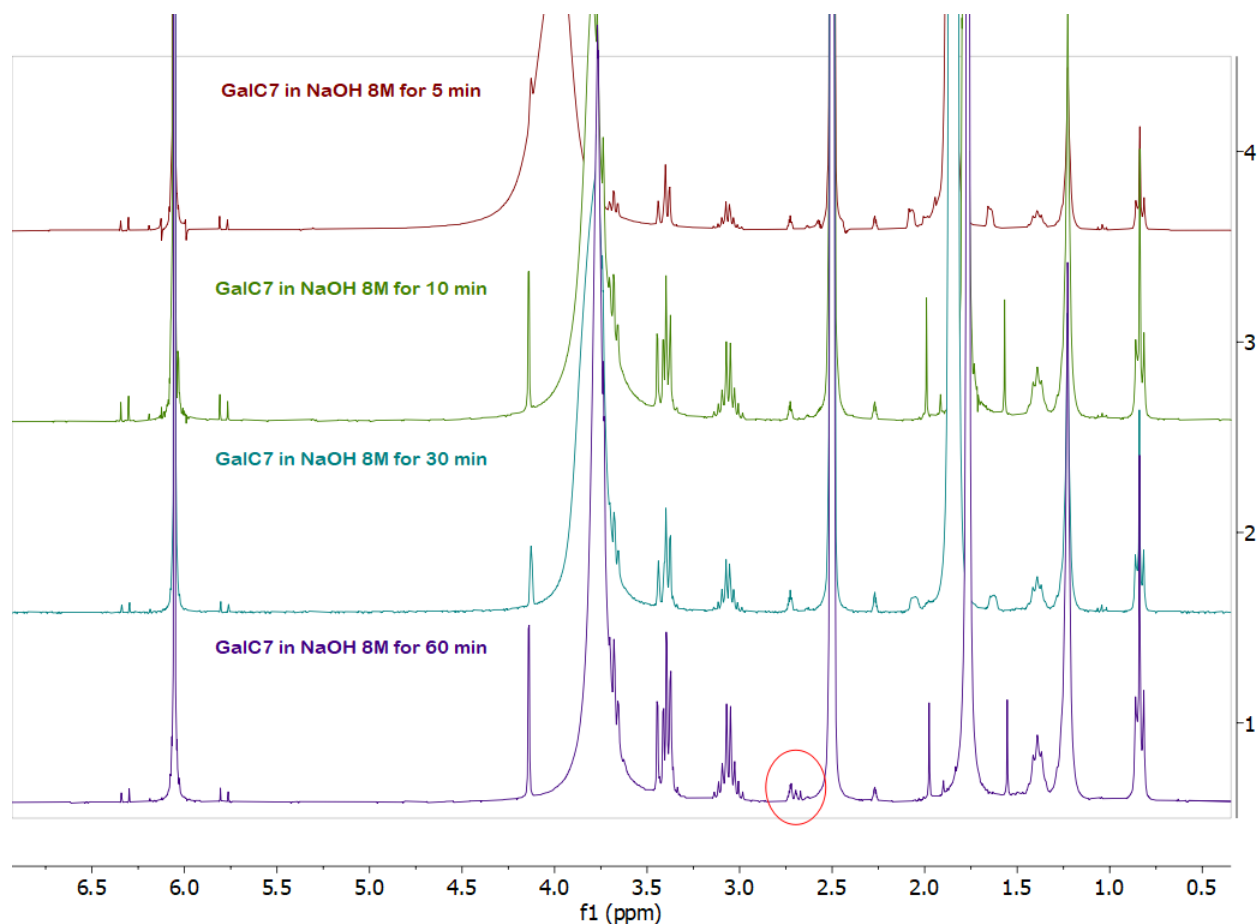


Fig. SI-2. NMR spectra of N-heptyl-D-galactonamide in NaOH 8 mol.L⁻¹ in D₂O/DMSO-d₆ at different time, with maleic acid as an internal standard. After 60min, small peaks corresponding to the formation of heptylammonium are observed at 2.7 ppm.

SI-3 Phenol red color switch with different GalC7 concentrations

Preliminary experiments have been made to adjust the GalC7 concentration in the range where a well-shaped filament is formed and no clog at the needle, for $[HCl] \leq 2 \text{ mol.L}^{-1}$. When the concentration of $HCl \geq 1 \text{ mol.L}^{-1}$, the impact of GalC7 concentration on the color change in the range from 0.22 mol.L^{-1} to 0.30 mol.L^{-1} is not significant. The curves of the color change as a function of HCl concentration and injection rate display the same trends whatever the concentration of GalC7 in this range (Fig. SI-3.1). At lower concentration in HCl, the dispersion of the data is higher, around $\pm 1 \text{ mm}$. In addition, a control experiment has been made without GalC7 (Fig. SI-3.2). The dispersion of the data is the same with GalC7 or without GalC7.

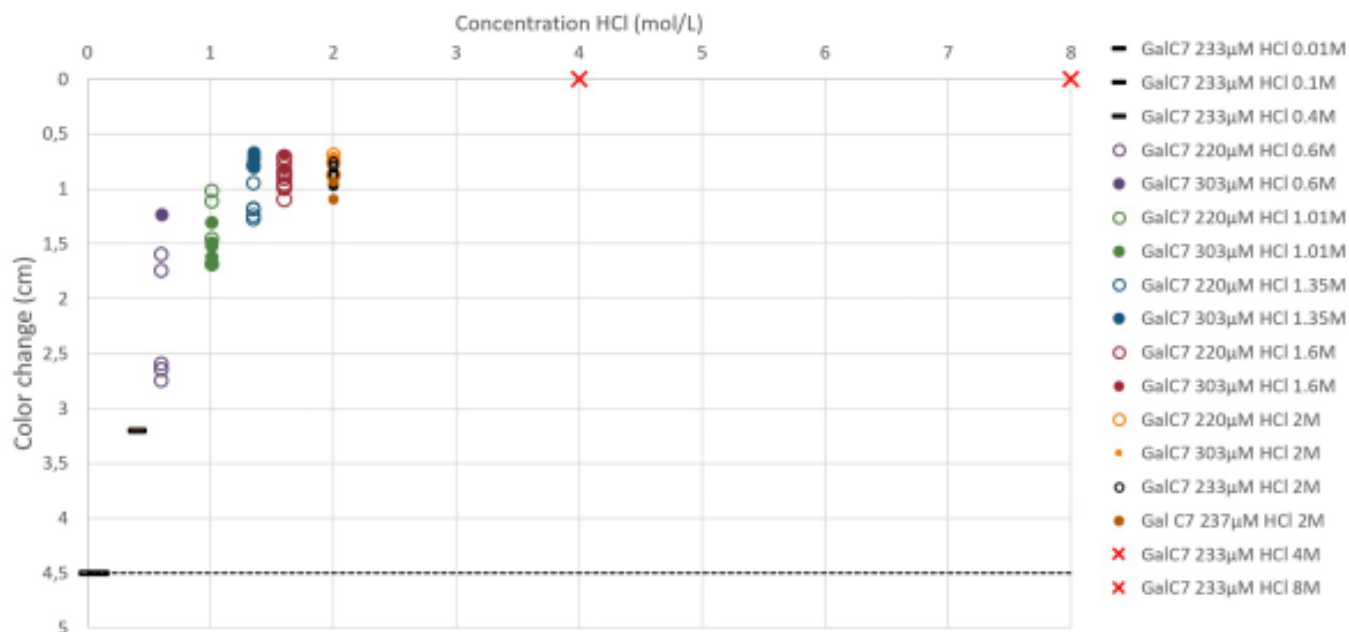


Fig. SI-3.1. Visualization of the color switch of phenol red (in a solution of GalC7 in NaOH 8M) injected in a bath of HCl at different concentrations.

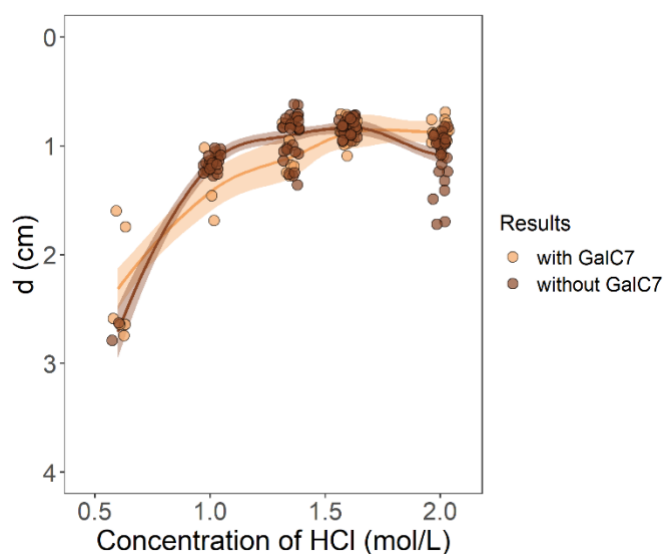


Fig. SI-3.2. Distance of the phenol red color change without GalC7 or with GalC7 (0.22 mol.L^{-1} , $5 \mu\text{L}/\text{min}$)

SI-4 Full data for the Fig.7 of main text

Fig. SI-4.1 and Fig. SI-4.2 correspond to Figs. 7(a) and 7(b) respectively, with the full data set, showing the dispersion of the data. The dispersion is likely to be related to fluid instabilities and/or pump cycling (documented in the pumps specificities).

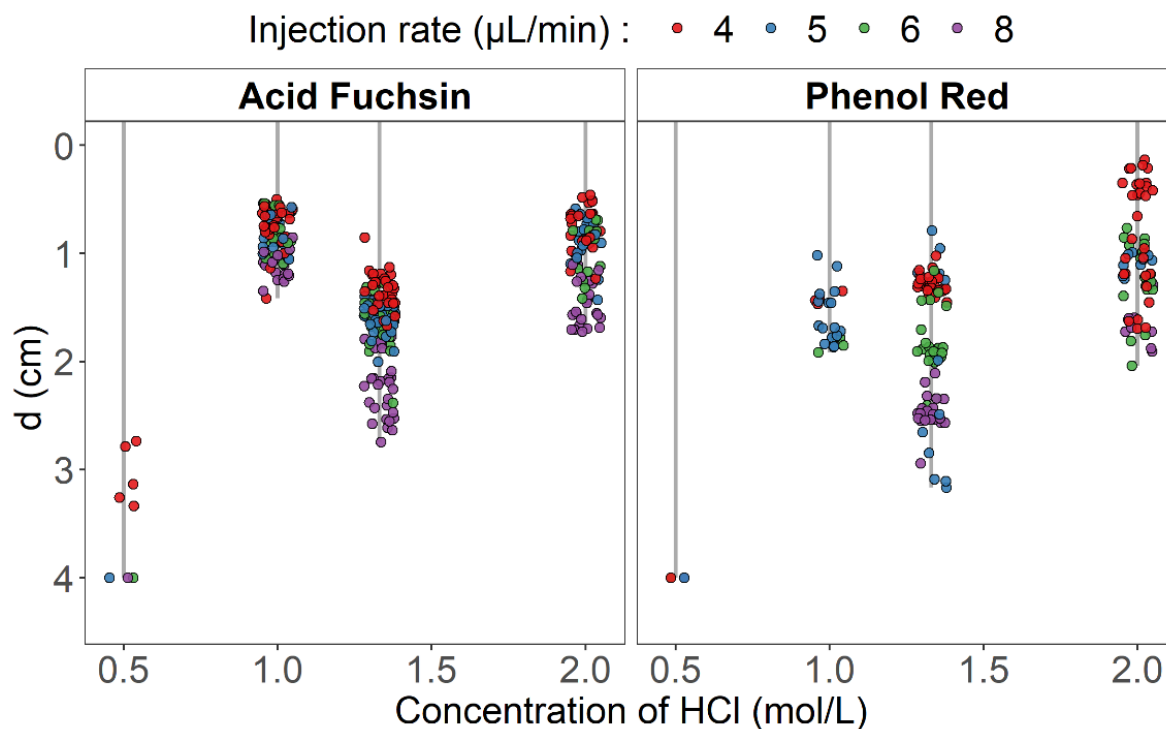


Fig. SI-4.1. Full data graph corresponding to Fig. 7(a). The set of data for each HCl concentration has been dispersed around the concentration value to enable the visualization of all the dots (jittered points representation). But all the measurements have been made at the exact HCl concentrations: 0.5 / 1 / 1.33 / 2 mol.L⁻¹. Detection of the color change point was much more difficult for HCl = 0.5 mol.L⁻¹, explaining that less data have been registered. When the jet reaches the bottom of the flask, it oscillates with a large amplitude and tends to bend. So it goes out of the focus plane. The color change is blurred and could have been detected only in few cases.

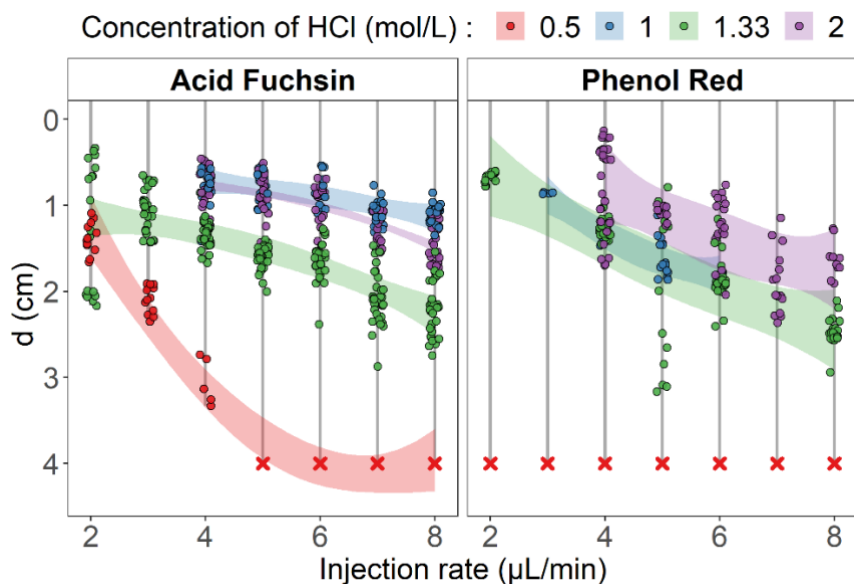


Fig. SI-4.2. Full data graph corresponding to Fig. 7(b). The set of data for each HCl concentration has been dispersed around the injection rate value to enable the visualization of all the dots (jittered points representation). But all the measurements have been made at the exact injection rates: 2 / 3 / 4 / 5 / 6 / 7 / 8 $\mu\text{L}/\text{min}$. The colored zones correspond to the 95% confidence interval. Red crosses correspond to conditions in which the color change does not occur before reaching the bottom of the vial.

SI-5- Selection of pH indicators of high pKa

Indicators have been selected according to their pKa, to their clearcut color change, a chemical structure prone to resist harsh basic conditions and their commercial availability. Indicators with high pKa are less common than medium range indicators. Their characteristics have been gathered here to select the most adapted to the wet spinning experiment.

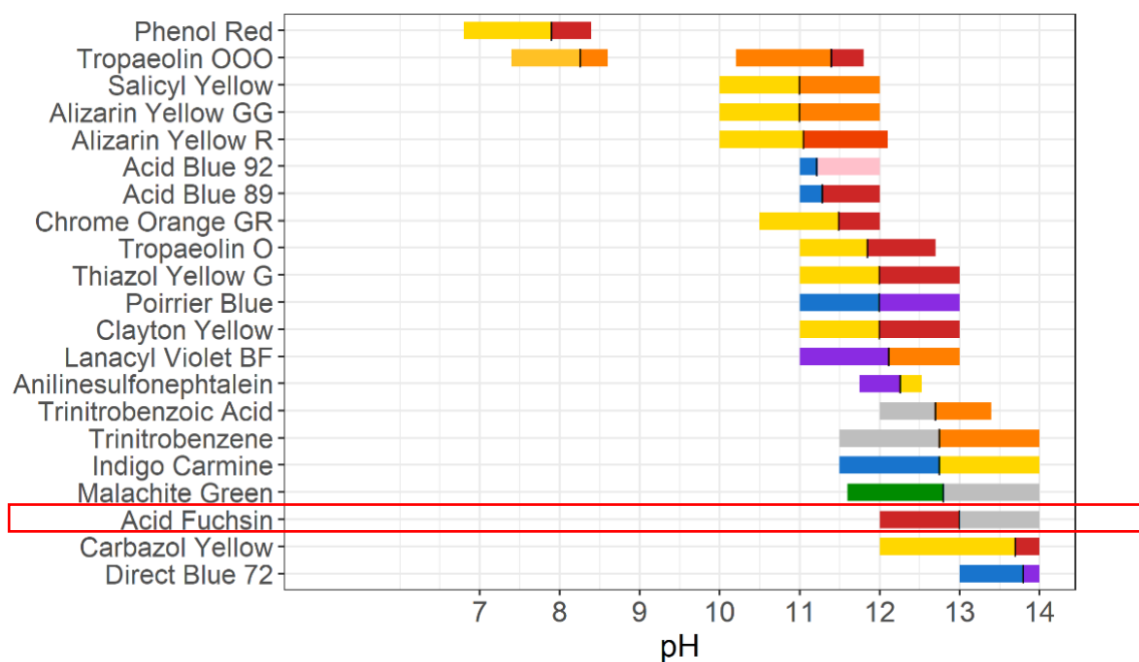


Fig. SI-5. pH indicators of high pKa and their color changes.

SI-6 – Calculation of the color change distance difference between acid fuchsin and phenol red

The term C_{OH}^d that has been neglected to plot the model curves from Equation (4) in Fig 8b ($C_{OH}^d \ll C_{OH}^0, C_{OH}^0 = 8 \frac{mol}{L}$, see below, eq. (4)), can be re-introduced in equations to check how large can be the difference of distance of color change between the two pH indicators, depending on the conditions of $[H^+]$ and D ,

Given d^{13} the distance of color change of acid fuchsin ($pK_a = 13, C_{OH}^d = 10^{-1} mol/L$) and d^8 the distance of color change of phenol red ($pK_a = 7.9 \approx 8, C_{OH}^d = 10^{-6} mol/L$), we use equation (4) to calculate the difference $d^{13} - d^8$:

$$\text{Equation (4)} \quad d = \frac{D C_{OH}^0 - C_{OH}^d}{S k[H^+] C_{OH}^0} \approx \frac{D}{Sk[H^+]}$$

$$\text{Equation (5)} \quad d^{13} - d^8 = -D \cdot \frac{(10^{-1} - 10^{-6})}{Sk[H^+] C_{OH}^0} \approx -D \cdot \frac{A \cdot 10^{-1}}{8}$$

We use the slope of the linear relationships in Fig 8b fitted with the experimental results to set the constant terms $A = \frac{1}{Sk[H^+]}$ of Eq. (4) (this slope depends on the HCl concentration set for each given experiment).

It provides the following difference $d^{13} - d^8$, in cm. The grey figures are conditions that have not been explored or that have not been obtained experimentally. This calculation illustrates that, according to this model, the difference of color change between the two indicators difference is too small to be observed ($d^{13} - d^8 < 1 \text{ mm}$) whatever the conditions.

[HCl] mol.L ⁻¹	2 μL/min	3 μL/min	4 μL/min	5 μL/min	6 μL/min	7 μL/min	8 μL/min
0,25	0,03886	0,05829	0,07772	0,09715	0,11658	0,13601	0,15544
0,5	0,01943	0,029145	0,03886	0,048575	0,05829	0,068005	0,07772
1	0,009715	0,0145725	0,01943	0,0242875	0,029145	0,0340025	0,03886
1,33	0,007305	0,0109575	0,01461	0,0182625	0,021915	0,0255675	0,02922
2	0,0048575	0,00728625	0,009715	0,01214375	0,0145725	0,01700125	0,01943
4	0,0024275	0,00364125	0,004855	0,00606875	0,0072825	0,00849625	0,00971

Table SI-6: calculated difference of distance of color change between acid fuchsin and phenol red, $d^{13} - d^8$, in cm (equation 5), as a function of [HCl] and injection rate (D , in μL/min).

SI-7- Calculation of k

In Figure 8b, the slope is $A = \frac{1}{Sk[H^+]}$. By introducing the relevant values of $[H^+]$ in each line, we obtained the value of $Sk = 2.57 \text{ cm}\cdot\text{mol}^{-1}\cdot\text{min}^{-1}$.

Then the section of the jet S is calculated by taking a jet diameter of around $150 \mu\text{m}$, worked out from the camera snapshots with a constriction factor of 2.33 (reduction of the jet at the nozzle exit). The diameter was calculated by averaging the diameter by image analysis over the entire jet length. The resulting section is $1.86\cdot 10^{-4} \text{ cm}^2$. It then gives: $k = 0.225 \text{ L}\cdot\text{mol}^{-1}\cdot\text{s}^{-1}$ after taking in account the conversion of the units (min to sec and cm^3 to L).

SI-8- 3D printing set up overview

